Cellulose Nanocrystals and the Depletion Interaction
Colloidal Liquid Crystals and Colloidal Crystals

Bachelorthesis

KARI-ANNE VAN DER ZON

Supervised by

JASPER LANDMAN
DR. ANDREI V. PETUKHOV
PROF. DR. WILLEM K. KEGEL

August 31, 2015

VAN 'T HOFF LABORATORY FOR PHYSICAL AND COLLOID CHEMISTRY

Utrecht University

ABSTRACT

In this thesis, the production of cellulose nanocrystals (CNCs) with an average length of 440 nm is reported, as well as the formation of tactoids of the cholesteric phase of the produced CNCs in the prescence and absence of dextran. Moreover, the sedimentation of hollow silica cubes into rotator hexagonal phases at the top of the sediments and rhombic phases lower in the sediments, both in the prescence and absence of CNCs, is shown through analysis of Small-Angle X-ray Scattering patterns.

Contents

Chapter 1

Introduction by means of a Dialogue

"Hey Kari-Anne! Can I sit next to you?"

"Of course! I haven't seen you for a while."

"Well, life is busy. How are you?"

"Good. Busy as well. I'm writing my bachelorthesis at the moment."

"Oh, what is it about?"

"It is about some colloids an..."

"Wait, wait, *colloids*?"

"Colloids are just small particles in some medium. Bigger than molecules, but still small. Let's say with at least one dimension between about one nanometer and one micrion. Actually, systems with discontinuities at distances between a nanometer and a micron are called colloidal as well. [1]

"Ok, colloids. So, what kind of colloids are you working with?"

"Ehm, actually I switched topics during the project. I started with cellulose nanocrystals, but later on I also did experiments with hollow silica cubes."

"Cellulose is from plants, right?"

"True. Cellulose is present in like all plant cell walls. Bacteria, algae and some sea animals called tunicates make it as well. The organisms make this really strong [2] polymer by joining together β-glucose units via a kind of chemical reaction called condensation polymerization. And then these polymer chains attract each other because they have hydrogen bonding groups and form ordered, or crystalline, structures. However, some of the chains do not order and between the crystalline parts amorphous parts are present. [3] [4]"

"And how did you make the colloids out of the cellulose?"

"Using a quite old recipe. For more than sixty years [5], scientist have dissolved the amorphous parts with acid in order to get negatively charged crystalline rods that can form stable suspensions. [6] We call the rods nanocrystals, but others call them nanowhiskers, nanofibres [3], crystalline nanoparticles [6] and formerly microfibrils [7]."

"That must be confusing."

"It is. Luckily the hollow silica cubes are only known under one name. They are really something new, only in invented a few year ago [8] in the group where I'm doing the project. People make them by first preparing pseudocubic particles of hematite, an iron oxide. Then they coat them with silica and remove the hematite core. The resulting particles are not really cubic, actually. [9] Ever heard of superballs?"
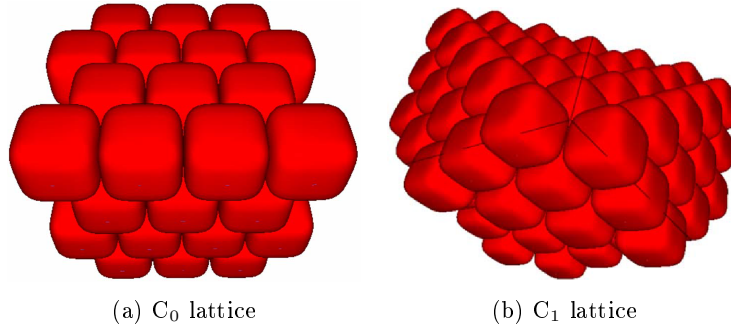
"Sounds like a toy."

(a) C_0 lattice   (b) C_1 lattice

Figure 1.1: C_0 and C_1 lattice packings of superballs. Reproduced from [11].

"It's a shape you can describe with this mathematical expression that works both for spheres and cubes. The hollow silica cubes are cubic, but with rounded edges. They are really cool because they can form all kinds of structures, even this very rare simple cubic structure [8] ... You look difficult, are you still following?"

"Ehm, I was wondering how the tiny cubes can form ordered structures. Do they attract or something?

"No, they even repel."

"Seriously?"

"Yes. All negatively charged. They order because of the concentration. If the concentration of particles is high enough, the particles all have more space if they are in an ordered structure. When they crystallize they win in what is called free-volume entropy."

"Wait, I know something about entropy, but I always thought that becoming ordered meant losing entropy."

"Yeah, you're right. The particles loose in configurational and/or orientational entropy upon ordering, but they gain so much free-volume entropy that they spontaneously crystallize." [10]

"If the concentration is good, isn't it?"

"You got it! One of the simplest ways to make the concentration right is by sedimentation. [10] Gravity pulls the cubes down. However, one of the features of colloids it that they possess intrinsic motion, Brownian motion. That counteracts gravity. [10] It's kind of a battle."

"Gravity vs. Brownian motion. Who wins?"

"They balance. The result is a concentration gradient. At the bottom there are many particles packed together and at the top there are only few. At the right concentration, the particles crystallize, into the interesting structures."

"How do you know the structures?"

"Well, first people performed simulations to find the densest structure superballs can possibly form. The researchgroup of Jiao found that, depending on the roundness of the corners, one of two crystal lattices, named C_0 and C_1, is the densest packing for superballs. Both lattices can be obtained by deformation of a face centered cubic packing, but the C_0 lattice possesses twofold rotational symmetry and while the C_1 has threefold." [11]

"Sorry, but those lattices are still not clear to me."

"I'll show you a picture." (see figure 1.1)

"Thank you. So... the superballs in both lattices have twelve touching neighbours. Am I correct?"

"Yes!" [11]

"Are these lattices only found from theory?"

"No, other research groups [12] [13] found by simulation that these C_0 and C_1 crystals are indeed the thermodynamically stable phases. Experimentally the C_1 phase was observed for several kinds of cubic-like particles." [14] [15]

"And do your cubes form that phase as well?"

"Well, Janne-Mieke, a former PhD student at our group investigated the structures formed by hollow silica cubes. She did not find the C_0 and C_1 lattices."

"Why not?"

"She found the two-dimensional analogs, the lattices named Λ_0 and Λ_1. [10] These were predicted by simulation in two dimensions. [16] [17] Janne-Mieke has induced crystallization of the cubes via various methods. Sedimentation was used for example. Now, sedimentation was carried out in glass capillaries. The cubes started to crystallize at the glass wall, forming layered structures. Within the layers, the particles ordered in two dimensions and formed these Λ_0 and Λ_1 lattices." [10]

"How did she find out?"

"Small-Angle X-ray Scattering, SAXS"

"And that is?"

"Ehm, it is a scattering technique. The crystal is radiated with X-rays. Then, the electrons in the crystal scatter radiation in all directions. However, the scattered rays interfere with each other. That works the same as visible light interference. Do you know what that is?"

"Yes."

"Because the structure is periodic, the interference is only constructive in a number of directions. [18] That results in a scattering pattern, from which the crystal structure can be determined. Actually, a scattering pattern from a crystal should be called a diffraction pattern. [19] The small angles had to be used because a colloidal crystal was investigated. The length scales are much larger than the wavelenght of the X-rays. Therefore, positive diffraction occurs in directions that make a very small angle with the unscattered beam. You know what was really awesome? I went along to Grenoble to do SAXS as well."

"Cool! Did you also investigate the hollow silica cubes there?"

"Yes. We thought it interesting to research the effect of cellulose nanocrystals on their crystallization. Do you know what depletion interaction is?"

"Nope"

"Well, Daan Frenkel has come up with a really cool analogy explaining depletion interaction. [1] It goes like this. Imagine a room in a restaurant with tables arranged in a typical dining set-up. At one night the room is booked for a party with many guests. What happens with the tables?"

"Ehm, they are pushed next to each other near the wall?"

"Indeed, because the people like to have more space. Now, this is what happens to the colloids as well. When they are surrounded by some smaller particles, called depletants, they are pushed together."

"So, in the analogy the cubes are the tables and the cellulose nanocrystals... the people?"

"Exactly! However, I told you I switched topics, right? In the beginning of the project the cellulose nanocrystals were the "tables" and dextran, a branched polymer of glucose units, [20] was used as a depletant.

"And did the cellulose nanocrystals crystallize as well?"

"Ehm, they did not sediment into crystals. Yet, they formed what is called a chiral nematic liquid crystal." [7]

"Huh, how can a crystal be liquid?"

"Crystalline means ordered, remember? True crystals consists of particles that are ordered in terms of orientation and position. Liquid crystalls are less ordered. For example, nematic liquid crystals only posses orientational order. They can consist of rods having their long axes pointing in the same direction. [21]"

 "And the cellulose nanocrystals align and form a nematic liquid crystal?"

"Almost, and when the formation of a liquid crystal of cellulose nanocrystals was first reported in 1959 [23], people thought it was nematic. But, it's chiral nematic, meaning that there is a twist in the orientation of the rods. The cellulose nanocrystals assemble into helicoids [7], say winding stairs.
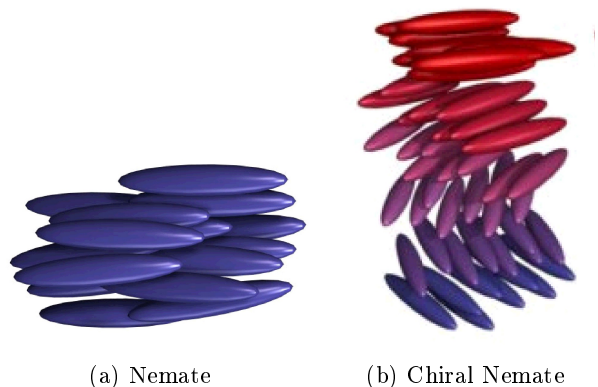
(a) Nemate   (b) Chiral Nemate

Figure 1.2: Schematic representations of liquid crystals of rods. Images reproduced from [22].

I'll show you an image of the liquid crystalline phases (see figure 1.2). The chiral nematic phase is sometimes called cholesteric because it was first recognized in suspensions of cholesterol." [21]
"But, if people already in in 1959 found this cholesteric phase of your particles, why did you make it again?"
"Well, the phase behavior of the cholesteric of cellulose nanocrystals was researched quite extensively [24] [25] [26] [27] [28] [29] [30], but it is still debated why the CNCs form a cholesteric phase instead of a nematic. Cellulose molecules are chiral, but it is not sure how this chirality is transferred to the colloidal length scale. [21] Some hypotheses involve a twisted shape of the nanocrystals [7] [31] [32], a twisted distribution of charges on the rods [7] or the presence of small amounts of cellulose oligomers at the surface of the nanocrystals. [21] In order to find the source of chirality, we intended to investigate the effect of perturbation on the chiral nematic phase. Our first step was to confine it spherically."
"How did you confine a liquid crystal?"
"When the cholesteric forms, droplets, called tactoids, in which the liquid crystal is confined spherically, arise. Tactoids of the CNC cholesteric phase are mentioned in a few articles. [7] [29] However, we added dextran as a depletant and we intended to do experiments with external fields and look at the coalescence of the droplets."
"And, what was the result?"
"We did make the tactoids. However, they are slow, too slow for a ten week project in fact. I did not do perturbation experiments nor wait for the tactoids to coalesce, but switched topics."
"And looked at the effect of CNCs on hollow silica cube crystallization, right? Did you write your thesis about both subjects?"
"Yes, the thesis comprises both systems. It has just the normal chapters, you know, theory, experimental, results, etcetera, but all chapters treat both experiments on the CNCs plus dextran and sedimentation of the cubes in prescence of the CNCs. The focus is more on the second system, though. The results chapter especially includes a long analysis of the SAXS data."
"Hey, I have to disembark at this station. Hmm, you still didn't tell what structures your cubes formed in prescence of CNCs. Anyways, it was really interesting to learn about your research."
"There really is a lot I didn't tell you. If you wish to know more about the project and the results, you should read my thesis."
"Yeah, would like to read it!"
"Cool. I'll send you a copy. See you!"
"Bye!"

Chapter 2

Theory

This chapter comprises four sections. The first section deals with the properties of the colloidal building blocks and the depletants described in this thesis. In the second section, general concepts governing the self-ordering of colloids are treated. The theory behind the research methods used in the project is explained in the third section and structures expected to be formed by the building blocks in prescence of depletants are described in the last section.

2.1 Building Blocks and Depletants

Research on two systems of building blocks and depletants is described in thesis. Cellulose nanocrystals are the building blocks and dextran polymers the depletants of the first system. In the other system, hollow silica cubes are the building blocks and the cellulose nanocrystals the depletants. The properties of cellulose nanocrystals, dextran and hollow silica cubes are described in this section.

2.1.1 Cellulose Nanocrystals

Cellulose is a β-1,4 linked polymer of glucose with a relatively rigid stucture. [33] The chemical structure of cellulose is presented in figure 2.1. Cellulose nanocrystals (CNCs) are rodlike colloids in which the cellulose chains are aligned due to hydrogen bonds. [20] The exact crystal structure of the CNCs can be found in literature, for example in [33] or [32]. Cellulose nanocrystals can be prepared by acid hydrolysis of a cellulose source, for example cotton. Natively, both crystalline and amorphous patches of cellulose are present. [3] [4] The amorphous parts are more loosely packed and dissolve faster in acid. Quenched acid hydrolysis with sulphuric acid results in cellulose nanocrystals with sulphate groups remaining. The negative charge of the sulphate groups enables the formation of stable cellulose nanocrystal suspensions. [34] [21] When the volume fraction is above a certain value, the suspensions spontaneously phase separate into an upper isotropic and lower anisotropic phase. The anisotropic phase is a chiral nematic liquid crystal. [7] This phase is described in subsection 2.2.4.
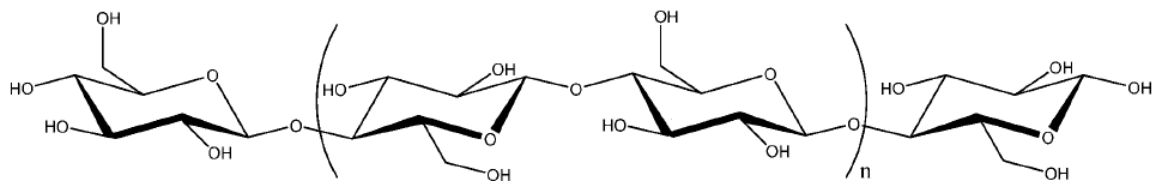
Figure 2.1: Molecular structure of cellulose. Figure adapted from [32].

2.1.2 Dextran

Like cellulose, dextran is a glucose polymer. However, it has a branched coil-like conformation. The glucose units are mainly linked via α-1,6 bonds, but some of the glucose units are connected to a third neighbour via α-1,3 linkages. This α-1,3 branching can be seen in figure 2.2.
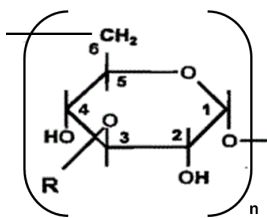
Figure 2.2: Molecular structure of dextran with an α-1,3 branched glucose unit, R. Figure adapted from [35].

2.1.3 Hollow Silica Cubes
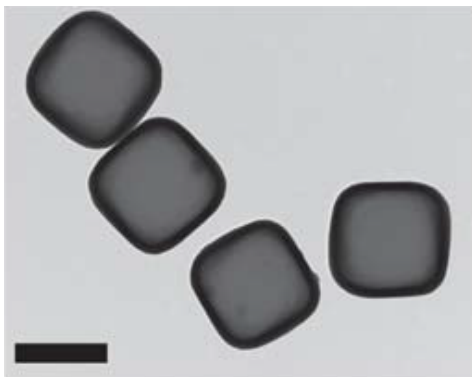
Figure 2.3: TEM image of hollow silica cubes with m=3.5. Scalebar is 1 µm. Reproduced from [36].

Figure 2.3 shows a TEM image of hollow cube-like colloids are made of porous silica. These colloids are called hollow silica cubes (HSCs). The porous silica has a density of about ρ=1.6 gcm^{-3}. [37] The

pH in all experiments described in this thesis was high enough to give the cubes a negative charge. Silica has a point of zero charge around pH 1.7-3.5. [38] The hollow silica cubes not technically cubic. The HSCs can be described quite well by the superball shape. However, in this thesis they are still called cubes.

2.1.4 Superballs and Superdisks

"Superball" is as well the generic term for a d-dimensional body as its 3-dimensional version. 2-dimensional superballs are called superdisks. [11] A d-dimensional superball is defined as a body that occupies in d-dimensional space the region:

$$|\frac{x_1}{r}|^m + |\frac{x_2}{r}|^m + ... + |\frac{x_d}{r}|^m \leq 1$$

Where m is the deformation parameter and r half the edge length. The deformation parameter indicates to what extent the shape deviates from a d-dimensional sphere. Spheres have a deformation parameter of 2 and cubes of ∞. [10] Figure 2.4 shows a selection of three-dimensional shapes as function of the deformation parameter. In literature other variables, such as p [16] [14] and q [12] [13] are used to describe the roundedness of superballs as well.

Figure 2.4: Three-dimensional superball shape as function of m. Figure reproduced from [9].

2.2 Self-Organisation of Colloids

Concentrated suspensions of colloids can spontaneously transform from fluid-like structures to those exhibiting long range orientational or spatial and orientational order: colloidal liquid crystals and colloidal crystals. [10] In this section factors influencing the crystallization of colloids are explained and structures of the liquid crystals and crystals mentioned further in the text are described. Furthermore, the crystal structures are described in reciprocal space and the use of Miller indices is introduced.

2.2.1 Depletion Interaction

Depletion interaction can promote self-organization of colloids. [9] The general mechanism responsible for depletion attraction is explained with figure 2.5. This figure represents colloids, depicted as grey
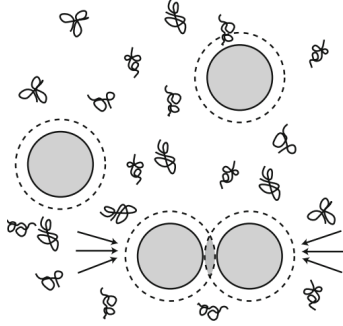
Figure 2.5: Schematic illustration of depletion interaction between colloids in presence of polymers. Reproduced from [1].

filled circles, in a solution of polymer chains. Around each colloid, there is a layer in which the centres of the depletants are unlikely to be found. This layer, called depletion layer is indicated by dashed lines in the figure. When the colloids are close together and the depletion layers overlap, the volume available for the depletants increases. This is entropically beneficial. Therefore, there is an attraction between the colloids. For small depletant concentrations, this attraction equals the product of the osmotic pressure of the depletants and the overlap volume of the depletion layers. The following expression is called the Asakura-Oosawa-Vrij (AOV) depletion potential:

$$W_{\text{dep}}(h) = \left\{ \begin{array}{ll} 0 & \text{if } h \geq 2\delta \\ \text{-}\Pi V_{\text{ov}}(h) & \text{if } 0 \leq h \leq 2\delta \\ \infty & \text{if h<0} \end{array} \right\}$$

with h the distance between two colloids and δ the thickness of the depletion layer. [1] In section 8.1.3, AOV depletion potentials are estimated for cylindrical colloids in the prescence of ideal polymers and cubic colloids in the prescence of hard rods.

2.2.2 Sedimentation

Sedimentation can induce self-assembly of colloids as well. [10] Sedimentation of colloids is counteracted by Brownian motion. This leads to a concentration profile in equilibrium. The concentration profile in a column of colloids in eqilibrium can be described by a Boltzmann distribution. The distance between the bottom of the column and the height at which the concentration is a factor e lower than at the bottom is called the gravitational length. In fact, it is the average distance from the colloids to the bottom. [37] In section 8.1.2 the sedimentation lengths of simple models of the CNCs and HSCs are calculated. Perfect cellulose cylinders with a length of 440 nm and a radius of 5 nm have a sedimentation length on the order of centimeters. The sedimentation length of perfect hollow silica cubes with edgelengths of 1000 nm and silica layer thickness of 100 nm is on the order of microns. The cellulose nanocrystals described in this thesis do not sediment under gravity, the hollow silica cubes do.

2.2.3 Electrostatic Repulsion

The CNCs and HSCs in all experimental conditions described in this thesis possess negatively charged surfaces. Debye screening lengths of two aqueous electrolyte solutions, approximating media surrounding the HSCs in experiments described in this thesis are calculated in section 8.1.1. The calculated Debye screening lengths are on the order of 10^{-8} or 10^{-9} m. This means that the electrical double layers surrounding the HSC are small enough for the anisotropy of the particles to be apparent. The surrounding media of the CNCs are not well defined. Therefore the Debye screening lengths in systems of CNCs and dextran are not calculated.

2.2.4 Liquid Crystals of Rods

What is meant by rods in this text are , characterized by a length, L, and radius, R. Upon concentrating a dilute rod suspension for $\frac{L}{R} > 7$ the phase states schematically depicted in figure 2.6 will be encountered: the isotropic liquid state, the nematic and smectic liquid crystalline states and a crystalline solid state. [1] Only the isotropic and nematic phases are referred to further in the text. In the nematic phase, the rods only possess orientational order. Their long axes point in the same direction, called the nematic director.

The chiral nematic phase, shown in figure 1.2b, is a special case of the nematic phase. In contrast to the normal nematic phase, the director rotates helicoidally around a fixed axis in the chiral nematic phase. The phase is chiral because there are two directions in which the director can possibly rotate, left-handed and right-handed. The chiral nematic phase is also called the cholesteric phase because it was first found in cholesterol. [21]

Liquid crystals can be thermotropic or lyotropic. The phase transition into a thermotropic liquid crystalline phase is induced by a temparature change, while the phase transition into a lyotropic liquid crystal is brought about by a change in concentration. [39] The cholesteric phase formed by CNCs is lyotropic.

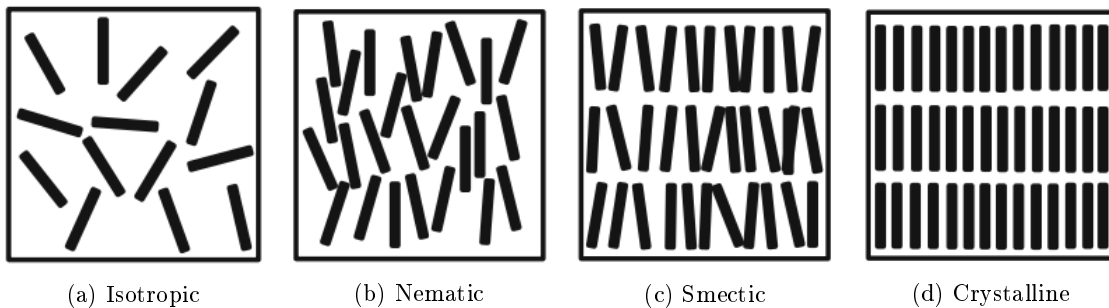(a) Isotropic   (b) Nematic   (c) Smectic   (d) Crystalline

Figure 2.6: Phase states of hard rod suspensions. Figure reproduced from [1].

2.2.5 Formation of Colloidal Liquid Crystals of Rods

The formation of a lyotropic nematic liquid crystalline phase in a relatively dilute suspension of rigid linear colloid was first explained by Lars Onsager in a 1949 paper [40]. Onsager demonstrated that

the isotropic-nematic phase transition spontaneously occurs due to a gain in free-volume entropy that compensates the loss of orientational entropy. The rod number density above which the nematic phase is entropically more favourable than the isotropic phase is on the order of $\frac{1}{L^2 R}$. [41] Multiplying this critical concentration by the volume of a single rod results in the critical volume fraction.

For typical CNCs, the critical volume fraction is on the order of 10^{-2}. However, the isotropic-liquid crystalline transition of CNCs can not exactly be described by Onsager theory. The CNCs are charged and tend to form a chiral nematic phase instead of a nematic phase. Moreover, they are very poly-disperse, causing a wide range of number densities at which the two phases coexist. The prescence of depletants can lower the number density at which the isotropic-nematic phase transition occurs. [1]

2.2.6   Formation of Layered Crystals

When sedimented in glass capillaries with flat glass walls, cubic colloids may form layered structures. The layeres are formed when the cubes anchor at the glass wall and orient with two faces parallel to the wall. If the capillary is thin with respect to the cube diameter, the wall anchoring in expected to have a strong effect on the overall structure. [10]

2.2.7   Two-Dimensional Lattices of Superdisks in Real Space

Three two-dimensional phases of superdisks are shown in figure 2.7 and explained in this subsection: the rotator hexagonal, Λ_0 and Λ_1 phases.

(a) Rotator hexagonal phase   (b) Λ_0 phase   (c) Λ_1 phase
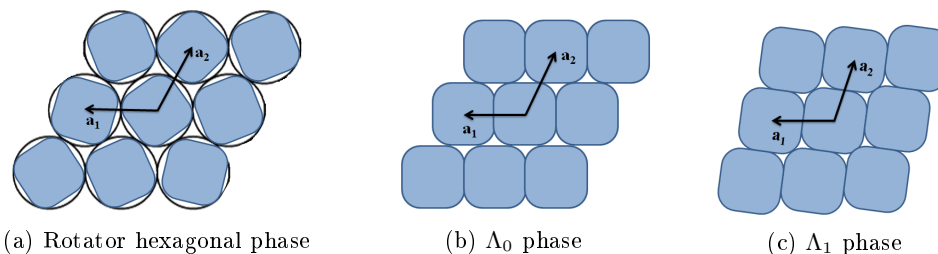
Figure 2.7: Rotator hexagonal, Λ_0 and Λ_1 phases of superdisks with lattice vectors $\vec{a}_1$ and $\vec{a}_2$ indicated.

Rotator Hexagonal Phase

Anisotropic particles in a rotator hexagonal phase, shown in figure 2.7a, are positioned in a hexagonal lattice. The particles can rotate freely around their centers of mass and effectively sweep circular areas. [17] The hexagonal lattice can be described by two lattice vectors of equal length, $\vec{a}_1$ and $\vec{a}_2$, that make an angle of 120 degrees.

Λ_0 Phase

The Λ_0 lattice, shown in figure 2.7b, consists of rows of particles that are offset by half the particle diameter. [10] It can be described by two lattice vectors, $\vec{a}_1$ and $\vec{a}_2$, with $\vec{a}_2 > \vec{a}_1$.

Λ_1 Phase

The Λ_1 lattice packing, also called rhombic lattice packing in this thesis, is shown in figure 2.7c. The lattice can be constructed from two vectors of equal length:

$$\vec{a}_1 = (2^{-1/m} - 2^{1/2}s)\mathbf{i} + (2^{-1/m} + 2^{1/2}s)\mathbf{j}$$

$$\vec{a}_2 = (2^{-1/m} + 2^{1/2}s)\mathbf{i} + (2^{-1/m} - 2^{1/2}s)\mathbf{j}$$

where $\mathbf{i}$ and $\mathbf{i}$ are unit vectors along the x_1 and x_2 direction, respectively. s is the smallest positive root of the following equation:

$$|2^{-(1+1/m)} - 2^{-1/2}s|^m + |2^{1+1/m} + 2 - 1/2s|^m = 1$$

Stacking of Λ_1 layers

In figure 2.8 three possible stacking fashions for Λ_1 lattices are shown. The centres of cubes in top site stacked layers are situated above each other. With bridge site stacking, overlying cubes lie on top of the corners of four underlying cubes. The centres of hollow site stacked cubes are located above the hollow between three underlying cubes. When the layers are stacked randomly, sliding planes are said to be present.

(a) Top site   (b) Bridge site   (c) Hollow Site

Figure 2.8: Possible stackings of Λ_1 lattices. Dots indicate the centres of the cubes in overlying layers.

2.2.8 Two-Dimensional Lattices of Superdisks in Reciprocal Space

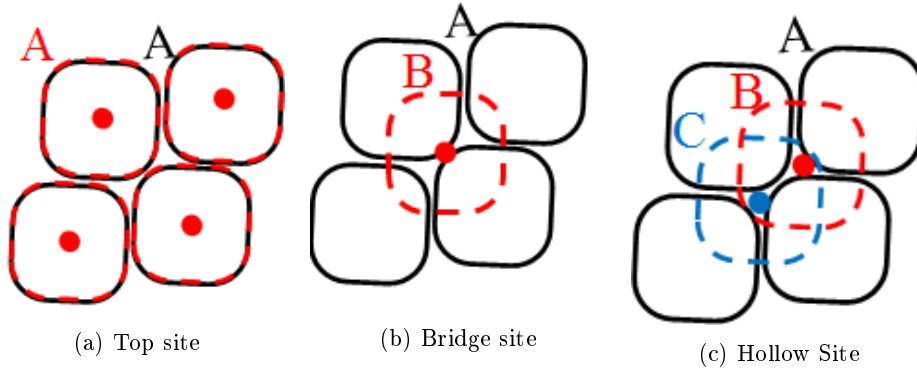In the following, some crystallographic concepts are mentioned and applied to the hexagonal and rhombic lattices. The two lattices are described in reciprocal space. Reciprocal space, a mathematical concept, is the space in which the Fourier transform of a spatial function is represented.

The periodic arrangement of the building blocks of a crystal can be described by unit cell vectors spanning a lattice. The points that are obtained by adding an integer number of unit cell vectors are called lattice points. Planes passing through lattice points are called lattice planes. [18]

Two-Dimensional Hexagonal and Rhombic Bravais Lattices in Reciprocal Space

The two-dimensional hexagonal Bravais lattice, of which an unit cell is shown in figure 2.10a, can be described by two unit cell vectors of equal length, $\vec{a}_1$ and $\vec{a}_2$ that make an angle of 120 degrees. The reciprocal of this lattice is described by $\vec{b}_1$ and $\vec{b}_2$. $\vec{b}_1$ makes an angle of 90 degrees with $\vec{a}_2$ and $\vec{b}_2$ makes a right angle with $\vec{a}_1$. Therefore, the angle between $\vec{b}_1$ and $\vec{b}_2$ is 60 degrees, as shown in figure 2.10b.

The rhombic lattice is very similar to the hexagonal lattice. The only difference is that the angle between $\vec{a}_1$ and $\vec{a}_2$ is between 90 ^{o} and 120°. The reciprocal unit cell of the rhombic lattice is similar to figure 2.10b, but the angle between $\vec{b}_1$ and $\vec{b}_2$ is larger than 60 degrees.
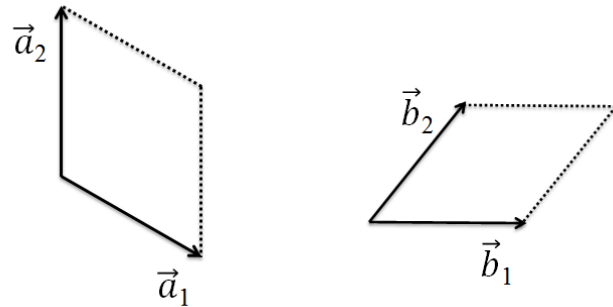
(a) Real space unit cell.   (b) Reciprocal unit cell.

Figure 2.9: Unit cells of the two-dimensional hexagonal Bravais lattice and corresponding reciprocal lattice.

2.2.9 Miller Indices

Lattice planes in two-dimensional lattices can be labeled with two Miller indices, the integers h and k. If a series of lattice planes divides $\vec{a}_1$ in h sections and $\vec{a}_2$ in k sections, the series of planes is labeled hk. The perpendicular distance between two consecutive planes in a series of lattice planes is called the lattice spacing d_{hk}. The vector $\vec{d}_{hk}$, perpendicular to the lattice planes with length equal to the lattice spacing can be used to define lattice planes.

The relationship between the lattice planes and the reciprocal lattice is given by:

$$\frac{\vec{1}}{d_{(hk)}} = h\vec{b_1} + k\vec{b_2}$$

Therefore, a series of lattice planes (hk) defined in the real space lattice can be represented by one point (hk) in the reciprocal lattice. [18] As an example, this is illustrated for three lattice planes in the hexagonal lattice and corresponding points in reciprocal space in figure 2.10.

(a) 10, 01 and $\bar{1}1$ lattice planes of the real space lattice.

(b) 10, 01 and $\bar{1}1$ points of the reciprocal lattice.
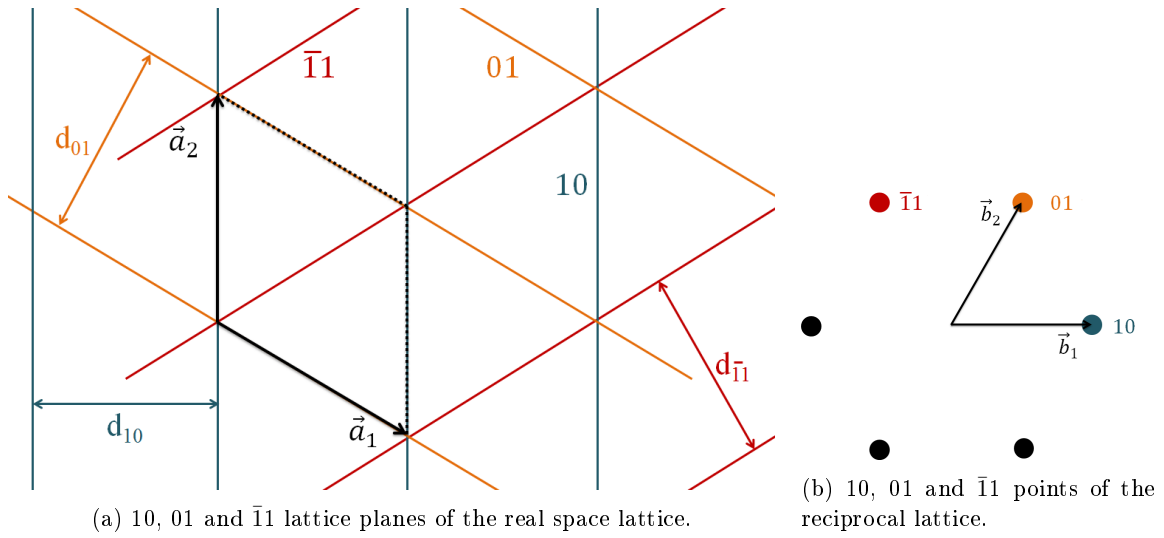
Figure 2.10: Miller indices indicated for lattice planes in real space and corresponding points in reciprocal space for the two-dimensional hexagonal Bravais lattice.

2.3   Research Methods

Both cellulose nanocrystals and hollow silica cubes are characterized by transmission electron microscopy. The system of CNCs in the prescence of dextran is researched using microscopy with crossed polarizers. The hollow silica cubes in the prescence of CNCs are investigated using small angle x-ray scattering.

2.3.1   Transmission Electron Microscopy

In a Transmission Electron Microscope electrons travel through a sample and are collected at the rear side. This resluts in a two-dimensional projection of the three-dimensional sample. [42] Electron blocking parts of the sample appear black on this projection.
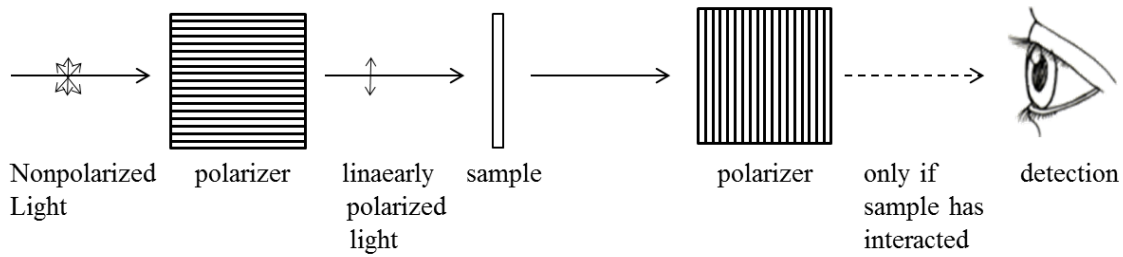
Figure 2.11: Crossed polarizers

2.3.2 Microscopy with Crossed Polarizers

Figure 2.11 illustrates how two polarizers can be used to visualize a sample that alters the polarization of light. The light arriving at the sample is linearly polarized due to the first polarizer. The second polarizer is rotated 90° with respect to the first one. Therefore, when the sample does not alter the polarization of the incoming light, there will be no light passing through the second polarizer. Cellulose nanocrystals aligned perpendicular to the direction of observation show birefrigence. They refract the incoming polarized light into two orthogonal polarizations. One of the polarizations is parallel to polarization direction of the second polarizer, and can pass through this polarizer. When the axis of the chiral nematic is approximately perpendicular to the direction of observation, the liquid crystal is periodically birefrigent and not birefrigent along the axis. Figure 2.12 shows how a striped pattern results from the helical ordering of the particles in the cholesteric. [21]
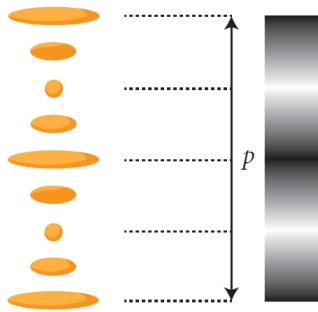
Figure 2.12: The alignment of the nanocrystals is periodically perpendicular and perpendicular to the direction of observation, causing a striped pattern. p stands for pitch and the direction of observation is from left to right. Figure reproduced from [21].

Using an optical microscopy setup in which two polarizers are placed as depicted in figure 2.11 chiral nematic liquid crystals can be identified and studied by the striped pattern.

2.3.3 Small Angle X-ray Scattering

In a SAXS set-up, a sample is irradiated with X-rays. The electrons in the sample scatter the radiation elastically. The scattered radiation is recorded and provides information in reciprocal space. Recorded SAXS patterns are usually represented as function of the scattering vector, $\vec{q}$. $\vec{q}$ is defined as the vector pointing from the wavevector of the incoming X-rays to the wavevector of the scattered rays. It's magnitude is given by:

$$q = \frac{4\pi}{\lambda} \sin\frac{\theta}{2}$$

with λ the wavelength of the X-rays and θ the angle between the incident beam and diffracted beam. [19]

Small angle X-ray scattering patterns recorded from colloidal crystals can provide information on the shape and size of the particles and the spatial configuration of the particles. [10] The particle form factor, $P(\vec{q})$, results from the intraparticle structure while the structure factor, $S(\vec{q})$, originates from the interparcticle structure. The scattered intensity, $I(\vec{q})$, is proportional to both the form factor and structure factor:

$$I(\vec{q}) \propto P(\vec{q})S(\vec{q})$$

2.3.4 Form Factor of a Superball

Figure 2.13a shows the theoretical two-dimensional form factor of an amorphous superball with m=3.6, oriented as shown in figure 2.13b. Two features are apparent from the figure, namely the cross shaped area of increased intensity and the anisotropic shape of the form factor maxima. The cross shaped intensity modulation is caused by the flat faces of the cubes. Faces parallel to the X-ray beam scatter most intense. The shape anisotropy is caused by the different dimensions within the cubes. The diagonals are longer than the edgelengths, resulting in shorter diagonal distances bewteen the form factor maxima and longer horizontal distances.

2.3.5 Form Factor of a Hollow Particle

In section 8.2.2, the form factors of a full sphere and hollow spheres with different wall thicknesses are calculated. For the spheres it is clear that with increasing hollowness, the form factor minima move to lower q-values.

Structure Factor of a Crystal

Crystalline structures give rise to intense spots, called Bragg reflections or peaks, at specific q-values. The scattering vector, $\vec{q}_{hk}$, describing a reflecion appears to be equal to the vector $\frac{\vec{1}}{d_{hk}}$ describing the lattice planes causing that reflection. The peaks appear because the waves scattered from the periodically ordered particles only interfere positively when Bragg's law is fulfilled:

$$2d\sin\frac{\theta}{2} = n\lambda$$

with d the distance between two subsequent lattice planes, θ the angle between the scattered and unscattered beam and n an integer. [18]
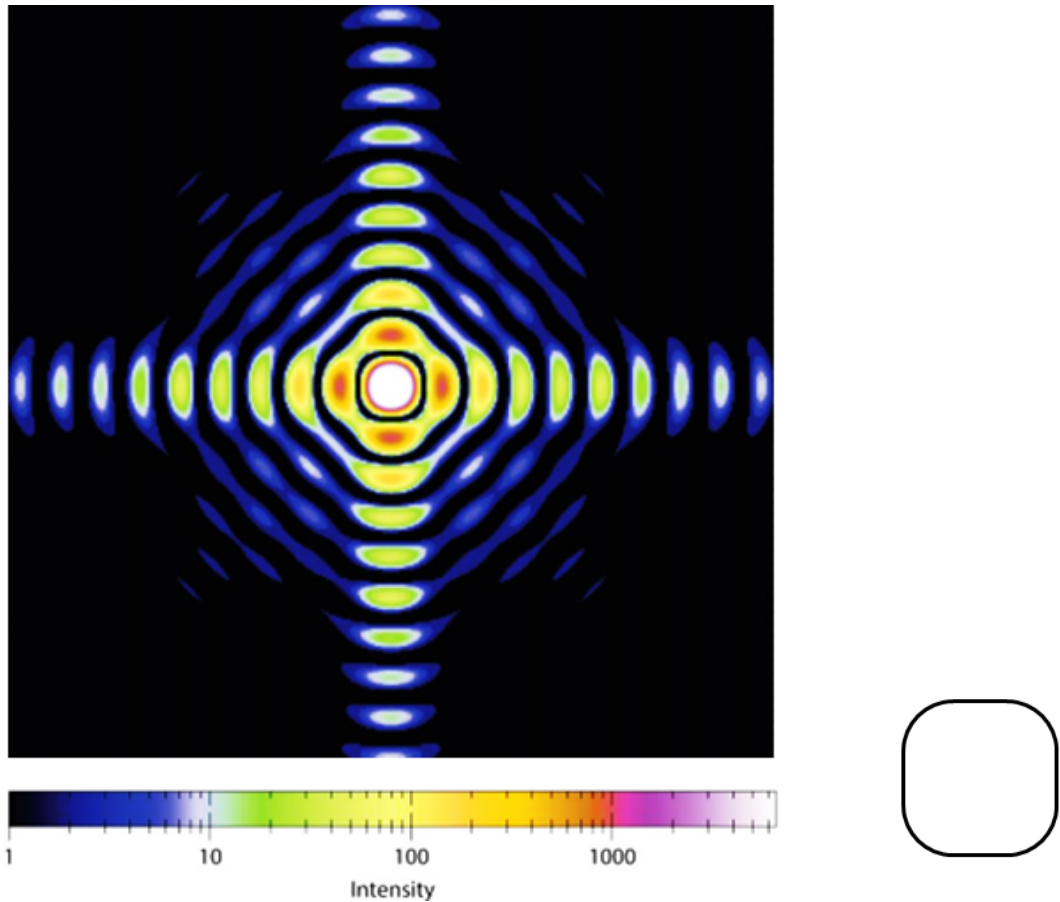
(a) Form factor calculated by Janne-Mieke Meijer (not yet published).   (b) A superdisk

Figure 2.13: Form factor of a superdisk oriented as depicted.

Relation between Lattice Spacings and q-Values of Corresponding Peaks

For first-order reflections, for which n=1, Bragg's law can be rearranged:

$$d_{hk} = \frac{\lambda}{2 \, sin\frac{\theta_{hk}}{2}}$$

The equation for the magnitude of the scattering vector, given on page 20, can be rearranged as well:

$$\frac{\lambda}{2 \, sin\frac{\theta_{hk}}{2}} = \frac{2\pi}{q_{hk}}$$

Therefore, the real space lattice spacing of lattice planes giving rise to a certain Bragg reflection can be calculated from it's q-value:

$$d_{hk} = \frac{2\pi}{q_{hk}}$$

The Third Dimension

The two-dimenional SAXS pattern can be influenced by the stacking of crystal layers. When rays scattered from different layers interfere negatively, peaks disappear from the scattering pattern. Figure 2.14, shows the 10 lattice planes in Λ_1 lattices of superballs stacked as described in section 2.2.7. For top site stacking, the lattice planes of all layers have the same periodicities. The scattering patterns resulting from top site stacked layers are the same as patterns resulting from a single layer. However, the periodicities of the 10 lattice planes of overlying layers are between those of underlying layers for brigde site and top site stacked Λ_1 lattices. This causes negative interference of waves scattered from the different layers and absence of the 10 peak from the scattering patterns. Similar reasoning can predict the absence of peaks emerging from other lattice planes. For example, $\bar{1}1$ reflections are absent on patterns recorded from hollow site stacked layers, but present in patterns recorded from bridge site stacked layers.

(a) Top site.   (b) Bridge site.   (c) Hollow site.
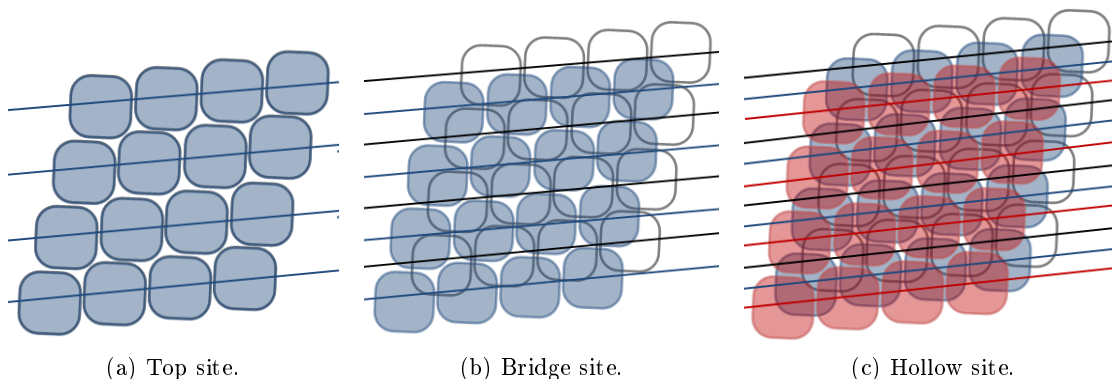
Figure 2.14: 10 lattice planes in top site, bridge site and hollow site stacked Λ_1 layers of superballs.

Bragg Rods

Three-dimensional information on the crystal structure can be extracted from rotation scans. During such scan the sample is rotated along it's vertical axis. SAXS patterns are recorded at several rotation angles, ω. ω is defined zero for the position in which the flat capillary wall is perpendicular to the beam.

Stacking disorder in scattering experiments manifests itself as the smearing out of some of the Bragg reflections along so-called Bragg scattering rods in the direction perpendicular to the planar stacking faults. [43] Whether Bragg rods are present or not can be found out from the rotation scans. Figure 2.15 schematically shows three Bragg rods in blue, viewed from the direction perpendicular to the crystal layers. From the figure, it can be deduced that if a Bragg rod is present, the x-position of the q_{hk} reflection as function of ω is described by:

$$q_x = \frac{q_{x,\omega_0}}{\cos\omega}$$
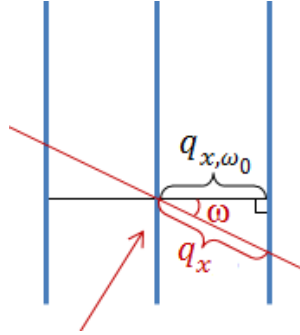
Figure 2.15: Increase of the horizonal q-value of a reflection by rotation of a random stacked sample by an angle ω. Bragg rods indicated by blue bars, horizontal axis of sample at ω_0=0 and ω by black and red line respectively and incoming beam indicated by a red arrow.

2.4 Previous Research

Previous theoretical, simulated and experimental work on systems similar to those described in this thesis is described in this section.

2.4.1 Experimental: Isotropic-Nematic Phase Transition of CNCs in presence of Dextran

In a 2002 paper [20], Edgar and Gray have shown that addition of blue dextran to CNC dispersions in the biphasic regime widens the biphasic regime and that the dextran preferentially partitions in the isotropic phase. Figure 2.16 shows the widening of the biphasic regime. Blue dextran contains nonionic covalently bound Recative Blue 2 dye randomly attached to the hydroxyl groups of dextran. [44] Edgar and Gray used 2000 kDa blue dextran and cellulose nanocrystals with an average length of 110 nm and diameter of 10 nm, prepared by acid hydrolysis of cotton paper.

2.4.2 Theoretical: Dense Packings of Superdisks

The Λ_0 and Λ_1 highly dense superdisk lattice packings were found from simulations by the group of Jiao [16]. For nearly all m-values, the densest packing is the Λ_1 lattice, as shown in figure 2.17.

2.4.3 Simulated: Phase Behavior of Rounded Hard Cubes

Avendaño et al. [17] simulated the phase behavior of rounded hard cubes. The group composed the outlines of the rounded cubes from four cylinders and four spheres. The cylinders of length L were used for the flat faces and the spheres of diameter σ for the rounded corners. The roundness of the corners is described by aspect ratio $L* = \frac{L}{\sigma}$. The simulations were performed as function of L^* and η, the packing fraction. η is the inverse of the packing density, ϕ, used by Jiao et al. [16]. Figure
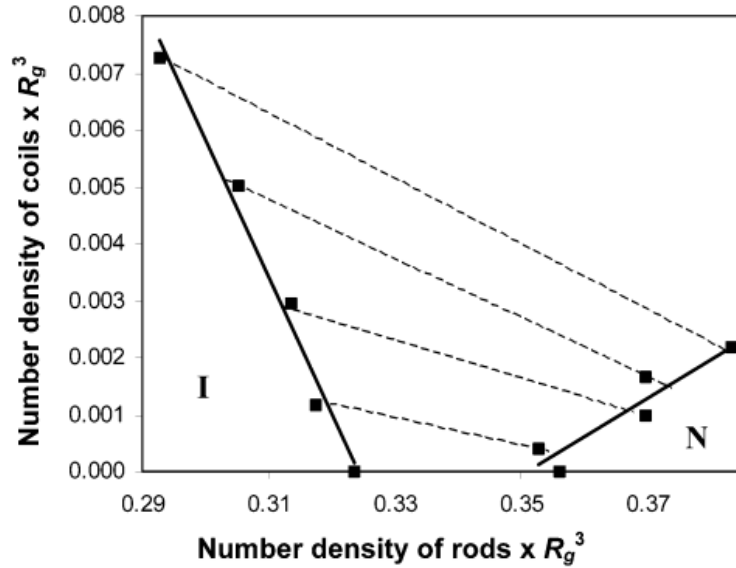
Figure 2.16: Partial phase diagram of a CNC suspension with blue dextran added. R_g is the radius of gyration of the dextran coil. I stands for isotropic region and N for the chiral nematic region. Figure reproduced from [20].

2.18 shows that for low η the rhombic phase, which is similar to the Λ_1 phase, was found. At higher packing fractions an rotator hexagonal phase was found.

2.4.4 Experimental: Layered Crystals of Hollow Silica Cubes

Evidence for the glass anchoring theory described in subsection 2.2.6 was provided from sedimentation experiments in which the cross-section of the capillaries was the only variable. Hollow silica cubes formed polycrystalline structures when sedimented in capillaries with circular cross-section and layered structures when sedimented in capilllaries with flat walls. [10]

Depletion induced crystallisation of hollow silica cubes may also lead to two-dimensional structures. As shown in figure 2.19, both the Λ_1 and Λ_0 as well as a simple cubic structure can form when hollow silica cubes sediment on a horizontal flat glass bottom at low cube concentrations in prescence of depletants. The q in the diagram is the size ratio $q = \frac{2R_g}{D}$, with R_g the polymer depletant radius of gyration and D the superdisk edgelength.
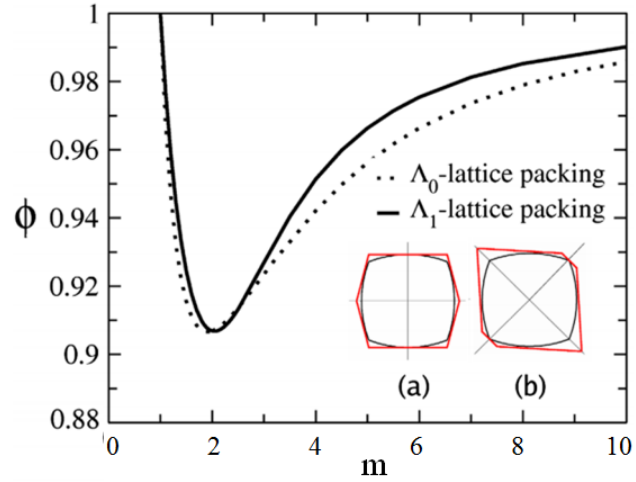
Figure 2.17: Packing denisty versus deformation parameter for the Λ_0 and Λ_1 lattice packings of superdiscs. Figure adapted from [16].
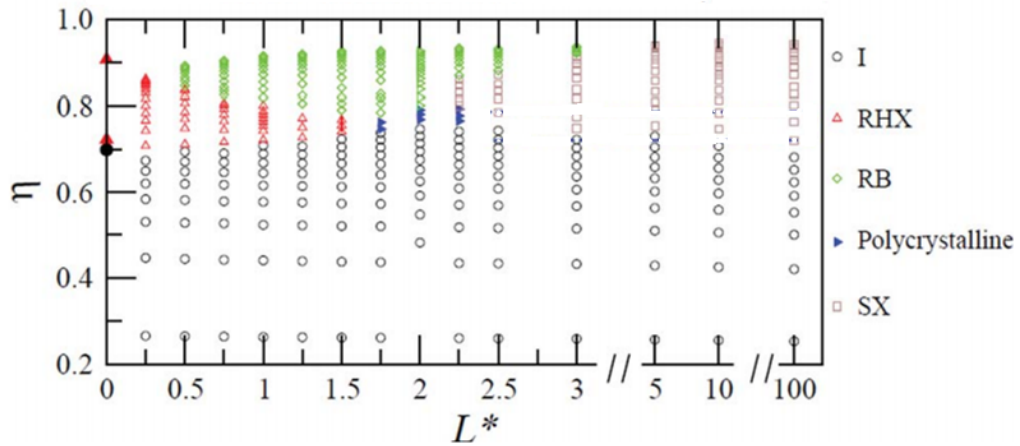
Figure 2.18: Simulated phases of rounded hard spheres as function of η and L^*. Figure adapted from [17].
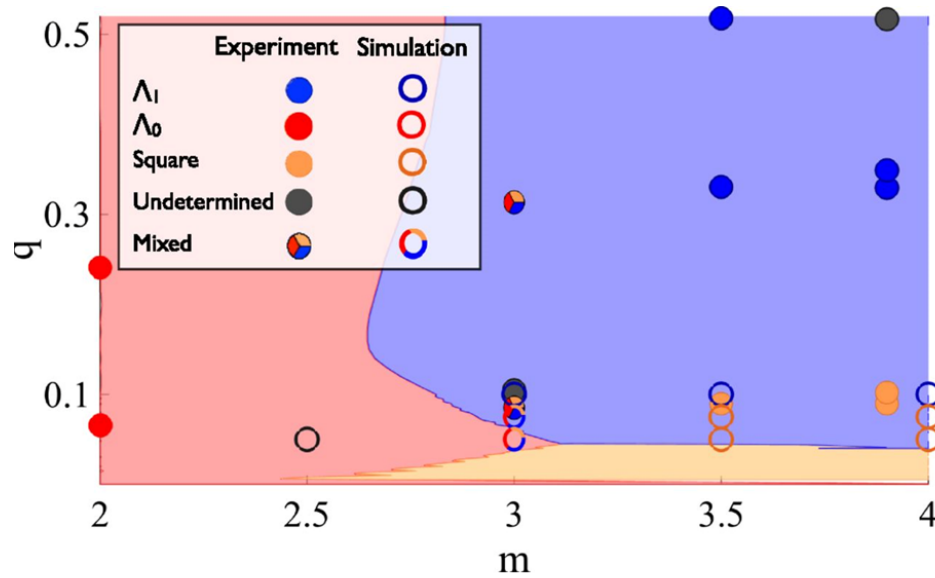
Figure 2.19: Comparison between experimental observations, bulk crystal simulations, and calculated phase diagram for superballs at different m and q values. Circles indicate the experimental results, open circles indicate simulation results, and the background colours indicate phases predicted by calculation. Figure reproduced from [9].

Chapter 3

Experimental

3.1 Materials

Details of the chemicals, laboratory items and hollow silica cubes mentioned in this thesis can be found in this section.

3.1.1 Chemicals and Laboratory Items

The water used in all experiments was purified by a Synergy Millipore system. The other chemicals mentioned in this thesis are listed in table 3.1. The laboratory items used in the experiments are specified in table 3.2.

Table 3.1: Chemicals

Name	Formula	CAS #	Purity	Supplier
Sulphuric acid	H_2SO_4	7664-93-9	96 %	ACROS
Rhodamine B ITC	$C_{28}H_{31}ClN_2O_3$	36877-69-7	Mixed isomers	Sigma-Aldrich
Sodium Hydroxide	NaOH	1310-73-2		
Dextran 70	$(C_6H_{10}O_5)_n$	9004-54-0		Applichem Lifescience
Sodium Azide	NaN_3	26628-22-8	99%	Fisher Scientific
Pleuronic F-127		9003-11-6	BioReagent	Sigma-Aldrich
Tetramethylammonium Hydroxide	$N(CH_3)_4OH$	75-59-2		
Sodium Chloride	NaCl	7647-14-5		

3.1.2 Hollow Silica Cubes

For all experiments with cubes described in this thesis, hollow silica cubes from one batch made by Janne-Mieke Meijer and Vera Meester were used. The synthesis was started with the production of hematite cubes according to the gel-sol method used by Sugimoto et al. [45]. This resulted in cubic

Table 3.2: Items

Item	Supplier	Specification	Catalog number
Filter paper	Whatman	Ashless clippings filter aids	1703-050
Filter	Sartorius stedim	Minisart NML syringe filters	16555
Microscope slide	Thermo scientific	British Standard Slides 76 x 7 mm	10144633AF
Spacer	VWR international	Cover glass # 0, 22x 22 mm	631-0123
Cover glass	Menzel Gläser	Coverslips # 1.5, 22 x 22 mm	BB022022A1
UV glue	Norland	Optical adhesive 81	
Capillary	VitroCom	VitroTubes 0.2 x 4.0 x 100 mm	3524

particles with an average edge length of 932 nm and a polydispersity of 5.5 % [46].Then the cubes were functionalized with polyvinylpyrrolidone and coated with amorphous silica using an adaptation of the Stöber synthesis. In a third step, the hematite cores were dissolved with hydrochloric acid. Details on the synthesis can be found in the PhD thesis of Janne-Mieke Meijer [10] or masterthesis of Vera Meester [46] .The hollow silica cubes used for the experiments described in this thesis had been stored in ethanol for two years.

3.2 Cellulose Nanocrystals

The cellulose nanocrystals (CNCs) were obtained by acid hydrolysis of cotton cellulose. A synthesis procedure based on a procedure from dr.Ahu Gümrah Parry was used. 20 grams of filter paper was cut into pieces of about half a centimeter by half a centimeter. The paper snippets, a stirring bean and 200 grams of 64 % sulphuric acid were put in a 2 liter bottle. The bottle was closed and for one hour it was put in a waterbath of 45 °C while the contents were stirred. Then, 1800 mL of water was added to quench the acid hydrolysis and the white dispersion was stirred shortly. The dispersion was left to stand overnight and it's clear top layer that was decanted. The bottom layer was centrifuged for half an hour at 3000 rpm. Subsequently, the supernatant was decanted again and the residue was redispersed in water. Two more times the dispersion was reconcentrated and redispersed in this manner. Then the dispersion was centrifuged for eight hours at 3750 rpm in order to make the cellulose settle out again. The supernatant was decanted and and the bottom layer was put in a piece of dialysis tube that had been in water for half an hour. The tube was put in a 2 liters cylinder with water that was refreshed twice a week. The pH of the water was measured every time before it was replaced. After one week the pH was 5 and it did not change till the cellulose was removed from the tube after three weeks. The cellulose was filtered with 1.20 µm filters and subsequently with 0.45 µm filters. Next, it was concentraded by centrifugation for two and a half hour at 17010 rpm. The gel was stored in the fridge.

3.2.1 Fluorescent Cellulose Nanocrystals

Fluorescent cellulose nanocrystals were prepared using the same procedure, but instead if adding water to quench the acid hydrolysis, 180 g of 1 M NaOH solution, 1 g of Rhodamine B ITC and 1620 g of water were added to the dispersion. The bottle was covered with aluminium foil to prevent photobleaching of the dye and its contents were stirred for three days. The dyed cellulose was concentrated by centrifugation for half an hour at 3000 rpm and redispersed in water twice. The dispersion was

centrifuged for half hour at 3750 rpm in order to reconcentrate. The supernatant was decanted and the residue was put in dialysis tube that had been immerged in water. The tube was put in a cylinder with water and the cylinder was covered with aluminium foil. The water was refreshed twice a week. After three weeks the pH had increased from 3 to 7 and the pink gel was filtered with $1.20\,\mu m$ filters. It was not possible to filter it with $0.45\,\mu m$ filters because filters would break when tried to use for filtering the gel. The gel was concentraded by centrifugation for two and a half hour at 17010 rpm and stored in the fridge.

3.3 Characterization

In this section experimental details on the characterization of the cellulose nanocrystals and hollow silica cubes are given.

3.3.1 Cellulose Nanocrystals

Small amounts of nonfluorescent and fluorescent CNC gel were weighted and heated under a heat lamp until the weights did not change anymore. Using this method, the weightpercentages of compounds that do not vaporize under a heat lamp were determined.

For transmission electron microscopy (TEM) a small amount of gel was put in a vial and diluted with water. A series of dilutions was prepared and a drop of each dilution was put on a polymer coated copper grid. The grid was put under a heat lamp till the droplet had vaporized. With a Philps-FEI Tecnai 10 transmission electron microscope the CNCs were made visible. Length determination of the nonfluorescent particles was performed with iTEM. Low contrast and clustering complicated imaging.

3.3.2 Hollow Silica Cubes

The shape and size of the hollow silica cubes were investigated with TEM. Since hollow silica cubes shrink upon illumination with an electron beam, [47] TEM was performed on silica coated cubes with the hematite cores still in it. It has been shown that dissolving the hematite cores does not alter the shape of the cubes. [47] TEM samples were prepared by drying a dilute drop of dispersion on a polymer coated copper grid under a heat lamp. 160 pictures of single cubes were made. With iTEM the edge length of the cubes was determined. A Matlab script written by William T. M. Irvine could fit the deformation parameter and aspect ratio of 120 of the pictures. The script fits the circumference of the two dimensional TEM projection according to:

$$|\frac{x}{r_1}|^m + |\frac{y}{r_2}|^m = 1$$

with r_1 and r_2 $(r_1 \geq r_2)$the semiaxes of the particle, $\frac{r_1}{r_2}$ the aspect ratio and m the deformation parameter.

3.4 Depletion Series of Cellulose Nanocrystals

In this section the preparation of a series of depletion samples with varying amounts of cellulose nanocrystals and dextran 70 are described. Also technical information on the polarization microscopy performed on the samples is given.

3.4.1 Depletions Samples

A set of vials was filled with sodium azide solution, water and varying amounts of CNCs and dextran 70. The sodium azide concentration in all samples was 0.02 wt%. It was aimed to vary the concentration of CNCs between 2.5 and 5 wt% in steps of 0.5 wt% and the concentration of dextran 70 from 0 to 3 wt% in steps of the same size. Only the depletion samples mentioned later on in this thesis are specified in table 3.3.

Table 3.3: CNCs and Dextran in Depletion Samples

Label	Cellulose Nanocrystals (wt%)	Dextran 70 (wt%)
A	5.03	0.00
B	5.02	1.31
C	5.01	1.77
D	4.48	1.40

3.4.2 Microscopy Slides

Microscopy slides of the depletion series were made a couple of days after the mixtures had been prepared. Each slide was made by glueing two spacers on top of a microscopy glass and pipetting a drop of the mixture in between. Then a cover glass was glued on top and the slide was put onder a UV lamp until the glue had polymerized.

3.4.3 Polarization Microscope

A Nikon Eclipse Ti-E inverted microscope equipped with a polarizer placed after the Nikon Intensilight C-HGFI lamp and a second polarizer, rotated 90 degrees with respect to the first, placed after the Nikon CFI Plan Fluor 40 x objective was used to make all polarization micrographs in this thesis.

3.5 Sedimentation Capillaries with Hollow Silica Cubes

This section comprises the preparation of the sedimentation capilliaries. X-ray experiments performed on the capillaries are described in a separate section.

Firstly, the hollow silica cubes in ethanol were centrifuged for 20 minutes at 1600 rpm. Then, the supernatant was decanted and the sediment was dispersed in water. Again, the dispersion was centrifuged

at 1600 rpm, now for 30 minutes, the supernatant was discarded and the residue redispersed. The dispersion was let to stand over night and the next day the top part was decanted, aiming to get rid of the smallest cubes. Once more, the particles were redispersed, centrifuged, disposed of supernatant and redispersed.

Then, Eppendorf tubes were filled with $500\,\mu L$ of the dispersion and centrifuged for 1 minute at 10000 rpm. The supernatant was removed with a pipette and a solution of pleuronics was added. The pleuronics solution was added because at the same time samples with polyethylene oxide, not described in this thesis, were prepared. Pleuronics is a commercial surfactant that is not expected to influence the phase behaviour. Depending on the tube, TMAH and/or CNCs were added or not. Water and sodium chloride solution were added to all tubes. The tubes were vortex mixed and placed in an ultrasonic bath. Table 3.4 lists the TMAH and CNC concentrations of the samples mentioned later on in this thesis. All samples contained 5 x 10^{-2} wt% pleuronics and 10^{-4} M NaCl.

Table 3.4: TMAH and CNCs in Sedimentation Capillaries

Label	TMAH (M)	Cellulose Nanocrystals (wt%)
1	0	0
2	0	2 x 10^{-2}
3	10^{-3}	0
4	10^{-3}	2 x 10^{-2}

Glass capillaries were filled with the samples and the ends were closed by melting and sealed with a drop of nailpolish. They were placed with their long axis vertically and within days the cubes in the samples listed in table 3.4 settled out in sediments that showed patches of iridescent colour. The iridescence is caused by Bragg reflections and indicates the prescence of long range order.

3.6 X-ray Experiments

Transmission X-ray Microscopy and Small-Angle X-ray Scattering were performed at beamline ID11 of the European Synchotron Radiation Facility (ESRF) in Grenoble, France. ID11 is a multipurpose, high flux, high energy, materials science beamline. [48] X-rays with an energy of 25 keV, or a wavelenth of 0.50 Å were used for all experiments and a the detector was a 16 bit CCD camera (Photonic Science, Xios II) with 4008 x 2671 pixels with a size of $9\,\mu m$ x $9\,\mu m$. A schematic overview of the beamline and the hutches is shown in figure 3.1.

3.6.1 Transmission X-ray Microscopy

For the TXM experiments, the samle and a set of compound refractive lenses were placed in experimental hutch 2 and the detector was placed in experimental hutch 3. The distance between the sample and the lenses was 1 m and the distance between the detector and the lenses was 50 m. The TXM set-up is shown schematically in figure 3.2.
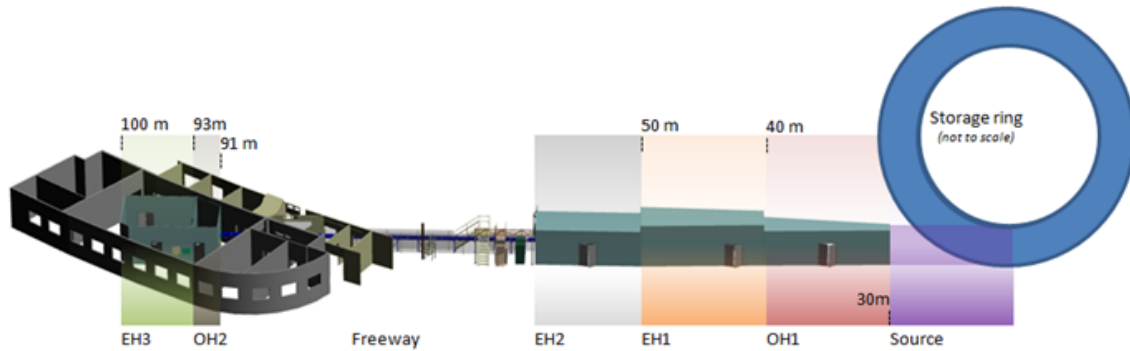
Figure 3.1: Overview of Experimental Hutches (EH) and Optical Hutches (OH) along Beamline ID11. Image reproduced from [48].
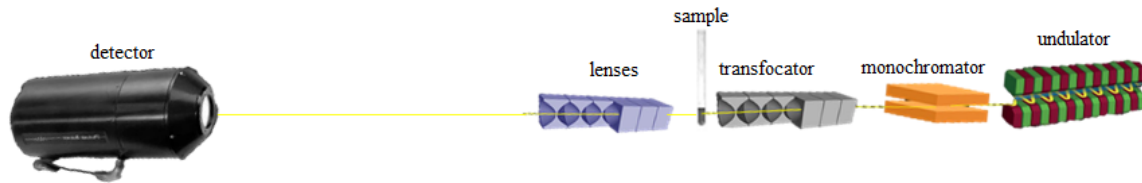
Figure 3.2: Illustration of the TXM set-up. Images adapted from [49], [50] and [51].

It was very hard to perform X-ray microscopy. The Siemens star was visualised succesfully and after some trying it was possible to observe the edges of the capillaries. Moreover, by taking 20 exposures at the same spot, adding their signal and dividing this signal by the signal of 20 added background exposures taken without sample, it was possible to discern features that resemble a lattice spacing, matching the lattice spacing expected in these samples. However, no useful information could be obtained from the X-ray microscopy data. Therefore, the TXM results are not discussed in chapter 4.

3.6.2 Small-Angle X-ray Scattering

Figure 3.3: Illustration of the SAXS set-up. Images adapted from [49], [50] and [51].

In order to do Small-Angle X-ray Scattering, the samples were placed in experimental hutch 3 on a distance of about 6 meters from the detector. The compound refractive lenses used for TXM were

removed and a beamstop was put in front of the detector. The detector could not be placed further away from the sample and only a small part of the detector was used. With their long axis vertically, the capillaries were placed on a stage that could move in x, y and z direction and rotate about the vertical axis. For normal incidence measurements, the direction of the X-ray beam was perpendicular to the flat faces of the capillaries. Scattering patterns were recorded from several heights in the sediments of samples. Rotation scans were made by rotating the capillaries in steps of 1° from a rotation angle, ω, of -70° to an ω of 70°, where the zero of ω is the normal incidence angle.

Microscopy slide D, described on page 30, was placed on the sample stage, but even with an exposure time of 65 seconds, no scattering was observed from the cellulose. On beamline ID10 with an X-ray energy of 8 keV and a smaller sample to detector distance no scattering could be noticed too. However, the sedimentation capillaries, described on page 31, would give rise to beautiful patterns, especially when recorded from iridescent coloured parts of the sediment. The results of the scattering experiments on the sedimentation samples are described in chapter 4.

3.6.3   Processing of SAXS data

One way of performing data correction is described by the following formula:

$$I_{\mathrm{S,corrected}}(\vec{q}) = (I_{\mathrm{S}}(\vec{q}) - DC(\vec{q})) - \frac{(I_{\mathrm{BG}}(\vec{q}) - DC(\vec{q}))}{(IC_{\mathrm{S}}/IC_{\mathrm{BG}})}$$

in which $I(\vec{q})$ is the recorded intensity as function of the scattering vector, S stands for sample and BG for background. Dark current, DC, is the intensity recorded by the detector when the X-rays are blocked from the experimental hutch. IC is the signal from the ion chamber, a device that measures the amount of X-ray radiation used in the experiments. [52] However, dark current was not measured, no ion chamber was used and information required for other kinds of extensive data correction, such as described in [53], was not collected. Therefore, background substraction was performed described by:

$$I_{\mathrm{S,corrected}}(\vec{q}) = I_{\mathrm{S}}(\vec{q}) - I_{\mathrm{BG}}(\vec{q})$$

Backgrounds were recorded from the liquid above the sediment. All SAXS patterns shown in this thesis were processed using a Mathemathica script written by Jasper Landman. After performing the backgroung substraction, the script would rescale the levels in the image to cover the range 0 to 1. Next, it would mulitply the values of all pixels by 10, raise it by 1 and take the ^{10}log of the result. Finally, the script would colour the pictures with Mathematica's 'SunsetColors'.

For quantitative analysis, the position of the beam centre was determined with Fit2d in 14 scattering patterns, using symmetry between reflections or the circular shape of from factor minima. The found position had a standard deviation of 0.5 pixel in the x-direction and 0.3 in the y-direction. Another script written by Jasper Landman was used to fit a multivariate normal distribution to any peak of interest and determine the position of its mean, as to calculate the q-values of the peaks and the azimuthal angles between the peaks.

Chapter 4

Results and Discussion

In this chapter results of the preparation and characterization of cellulose nanocrystals are discussed together with the results of the characterization of the silica cubes. Furthermore, tactoid formation in the depletion samples is shown through polarization micrographs. The main body of this chaper consists of analysis of the SAXS patterns recorded from the sedimentation samples at the ESRF.

4.1   Characterization

The gels of nonfluorescent and fluorescent cellulose nanocrystals produced as described on page 28 had a weight percentage of 10.6 ± 0.2 and 17.6 ± 0.9, respectively.

Figure 4.1a shows TEM images of the cellulose nanocrystals and a silica cube with hematite core. The length of the cellullose nanocrystals was determined to be $0.44 \pm 0.03\,\mu\text{m}$. This is large in comparison with average lengths of 90 to $300\,\mu\text{m}$ mostly found in literature. [7] [20] [26] [28] [54] [21] However, the dimensions of CNCs are known to vary widely, depending on cellulose source and reaction conditions used for their production. [24] [25] [32] For example, Edgar and Gray reported on cellulose nanocrystals with an average length of 110 nm, made with a very similar producedure. [20] An explanation for their shorter CNCs might be that they ground the filter paper before adding sulfuric acid.

The edgelength of the silica cubes was measured to be $1.046 \pm 0.007\,\mu\text{m}$. Using the Matlab script written by William T. M. Irvine, the aspect ratio between the two edgelengths in the plane of the picture and the m-value of the superdisks fitted to the projection of the silica cubes were determined to be 1.0042 ± 0.0030 and 3.5287 ± 0.0068 respectively. In real, the projections of the silica cubes are not exactly superdisk shaped. Because of the growth mechanism of the hematite cores [55] the space diagonals do not have the precise same length and the corners are not equally rounded.

34

(a) Cellulose nanocrystals

(b) silica cube with hematite core
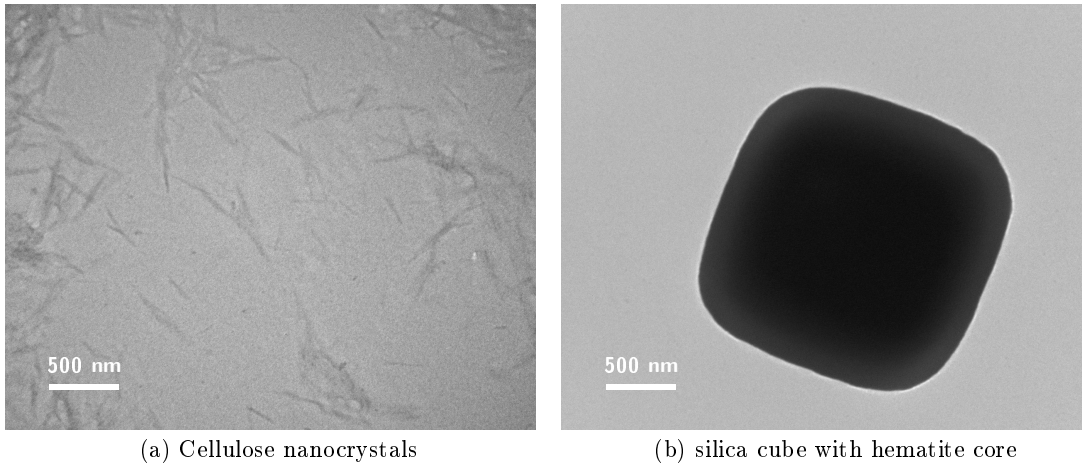
Figure 4.1: TEM pictures of cellulose nanocrystals and a silica cube with hematite core.

4.2 Tactoids

Using the polarization micropscopy setup described in section 3.4.3, the depletion samples described on page 30 were studied. Within 5 weeks after preparation tactoids were observed in samples A, B, C and D. After more than three months still no tactoids were discovered in samples with a cellulose nanocrystal concentration lower than 4.5 wt%.

4.2.1 Influence of Depletant Concentration on Tactiod Size

Whether tactoids form, how many tactoids form and the size of the tactoids formed appear dependent on the dextran concentration in the depletion sample, as can be seen in figure 4.2. None of the samples with a dextran concentration higher than 2 wt% gave rise to tactoids. Sample A without dextran, shown in figure 4.2a, is very crowded with tactoids. Figure 4.3 shows an decreas in tactoid size with increasing depletant concentration in samples A, B and C. We do not have an explanation for these observations. It is not known whether repetition of the experiments results in the same observations.

(a) No Dextran (A)	(b) 1.3 wt% Dextran (B)	(c) 1.8 wt% Dextran (C)
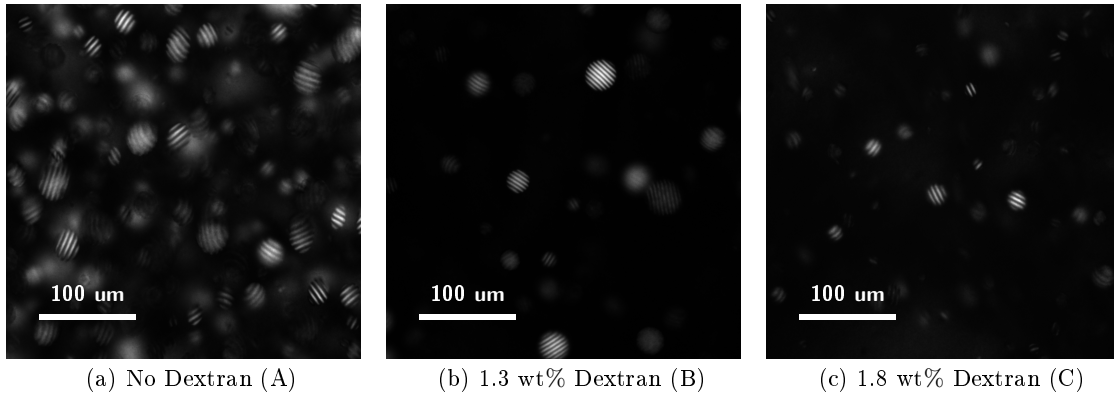
Figure 4.2: Polarization micrographs of tactoids from depletion samples A, B and C with different concentrations of depletant. Recorded 5 weeks after sample preparation.
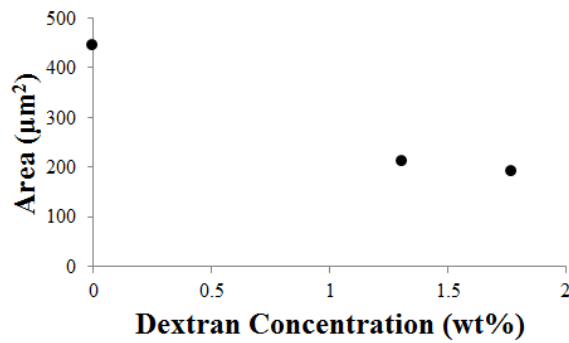
Figure 4.3: Avarage area of 2-dimensional projection of tactoid on polarization micrographs of samples A, B and C.

4.2.2 Growth of Tactiods

As can be seen in figure 4.4 the tactoids grow over time and the number of birefrigent bands seems to increase. However, no quantitative analysis was performed on tactoid growth.

(a) After 3 Weeks (b) After 4 Weeks (c) After 5 Weeks (d) After 3 Months
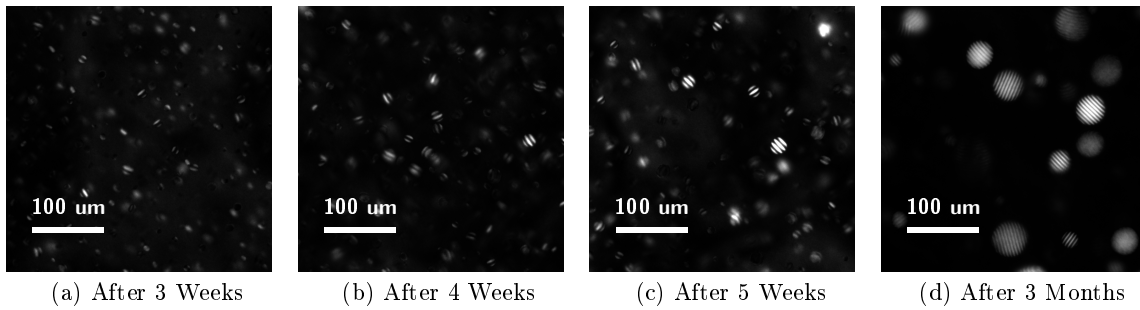
Figure 4.4: Growth of tactoids in time. Polarization micrographs of depletion sample D. Recorded at moments after sample preparation indicated.

4.3 SAXS analysis

Typical SAXS patterns from the sedimentation capillaries recorded and processed as described on page 32 are shown in figure 4.5. For each sample, the patterns are arranged in one column. The patterns placed higher in the figure are recorded at higher positions in the sediment, although the exact heights are not known. The wedge-shaped patch of zero intensity visible in each pattern is the shadow of the beam stop.

From this figure, it is clear that similar patterns are recorded from all samples. In this section the two dimensional structures that give rise to the patterns are deduced qualitatively, based on the patterns recorded from sample 4. The patterns are not treated in order of height, but in an sequence that is more convenient for explanation. The effects of TMAH and cellulose nanocrystals on the structures are treated in a separate subsection. Additionally, two rotation scans recorded from sample 4 and the three dimensional structure of the crystals giving rise to them are discussed.

4.3.1 No Order

Figure 4.6: SAXS pattern recorded at the bottom of the sediment of sample 4.

Figure 4.5: Overview of the typical SAXS patterns recorded from samples 1 to 4.

Figure 4.6 shows a diffraction pattern that is recorded typically from the bottoms of the samples. In this figure, no Bragg reflection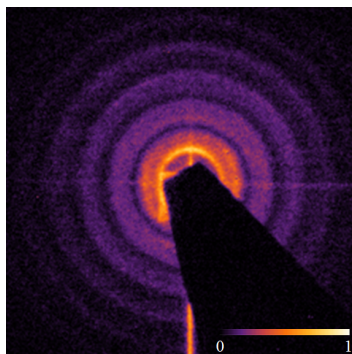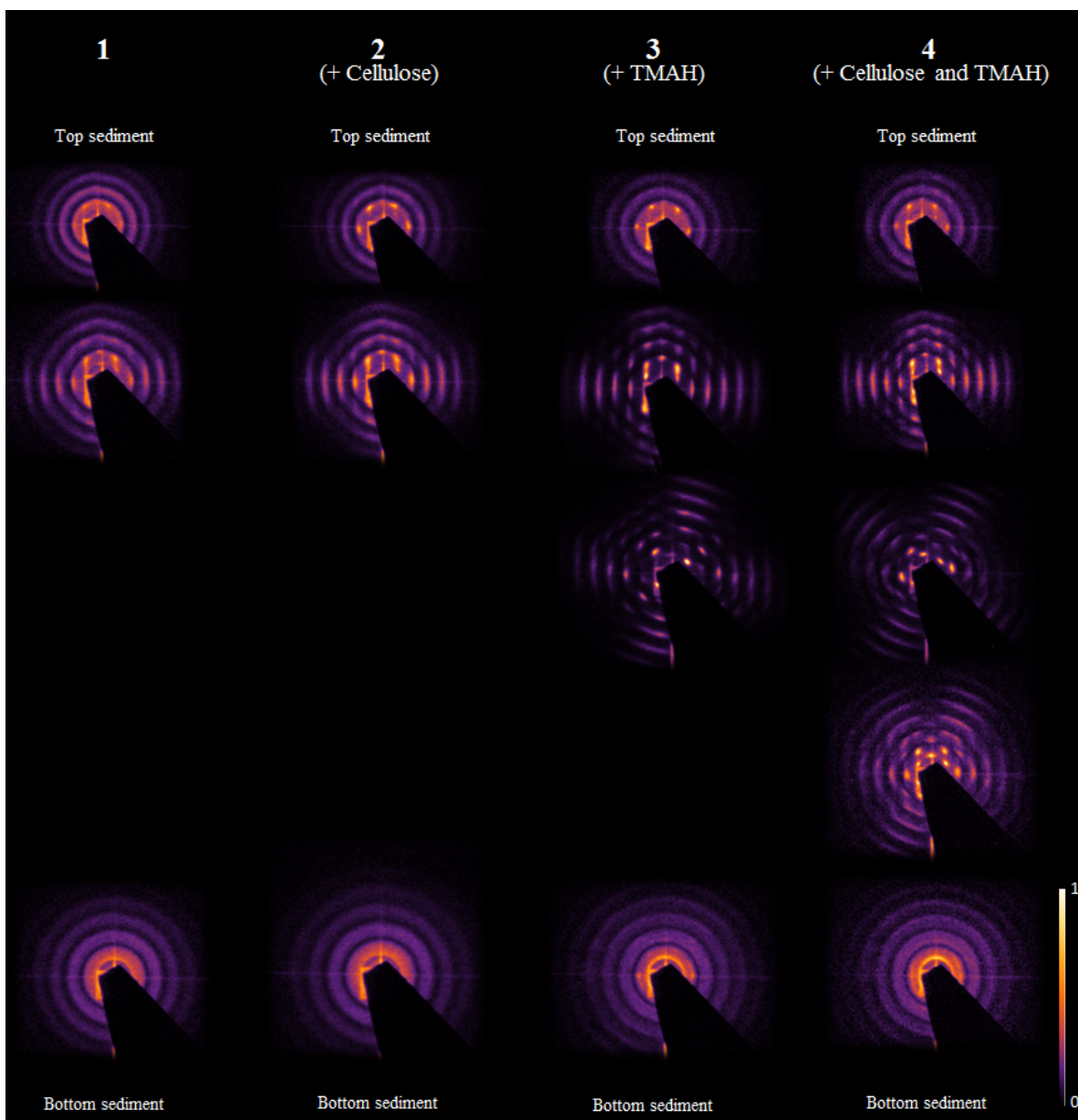s are visible, indicating an absence of long range order. As described on page 20, the hollow silica cubes used in the experiments should give rise to a cross-shaped form factor when oriented in the same direction. However, an isotropic form factor is visible. Therefore we can say that the cubes are oriented randomly. The prescence of isotropic phases at the bottoms of the samples can be understood from the fast compression of this part of the sediment. [10]

4.3.2 Rotator Hexagonal

(a) Diffraction pattern recorded from the top of the sediment of sample 4.

(b) Bragg reflections from 4.7a with reciprocal vectors $\vec{b}_1$ and $\vec{b}_2$ defined and Miller indices assigned.

(c) Real space hexagonal lattice with randomly oriented superdisks and real space vectors $\vec{a}_1$ and $\vec{a}_2$.
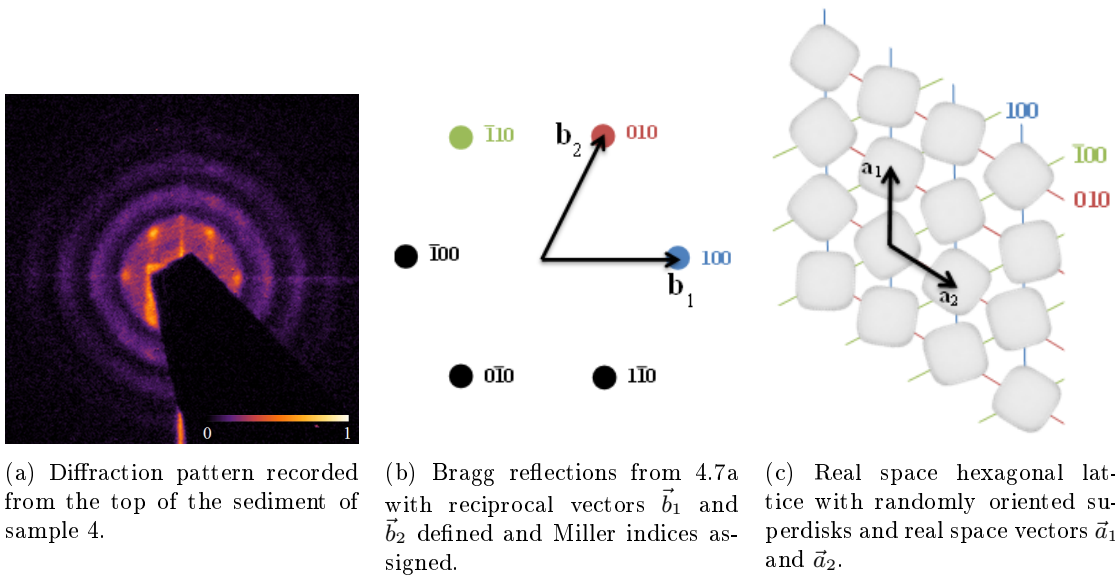
Figure 4.7: Rotator Hexagonal lattice assigned to pattern recorded from the top of the sediment of capillary 4. Reflections in 4.7b and corresponding lattice planes in 4.7c have the same colour.

Figure 4.7a is a typical SAXS pattern recorded from the top of the sediment. Like the patterns recorded from the bottoms of the capillaries it shows an isotropic form factor, indicating randomly oriented cubes. The clear diffraction peaks indicate long range order. Figures 4.7b and 4.7c explain schematically how a hexagonal Bravais lattice can be assigned to the diffraction peaks. The five reflections in 4.7a and a sixth reflection that would have been blocked by the beam stop are drawn in 4.7b. The six reflections can be described by two reciprocal lattice vectors, $\vec{b}_1$ and $\vec{b}_2$, defined as shown in the same figure, and Miller indices, also displayed, can be assigned to them. The angles between the 100 and 010 peak, the 010 and $\bar{1}10$ peak and the $\bar{1}10$ and $\bar{1}00$ peak found using the method described in subsection 2.2.9 are slightly less than 60 degrees. This is most probably because the analysis method is not precise enough. Symmetry would dictate the angle between the 100 and $\bar{1}00$ peak to be 180 degrees and we assume the aforementioned angles to be 60 degrees. From the reciprocal lattice vectors real space vectors can be calculated as described on page 21. The real space vectors $\vec{a}_1$ and $\vec{a}_2$ are drawn and the lattice planes that give rise to the 100, 010 and $\bar{1}10$ reflections are depicted in 4.7c in the colours of the corresponding reflections in 4.7b. The combination of hexagonal long range order and random orientation of the anisotropic particles can be explained by a rotator hexagonal phase, in which rotating cubes effectively occupy a spherical piece of space. We think it plausbile that at the

top of the sediment the pressure is low, that the hollow silica cubes can rotate and that they have formed rotator hexagonal phases, in line with the simulations described on page 23.

4.3.3 Rhombic

In this subsection, a pattern recorded from the middle of the sediment of sample 3 is analysed ahead of the pattern from sample 4 because it is more easy to interpret.

(a) Diffraction pattern recorded from the middle the sediment of sample 3.

(b) Brightest reflections from 4.8a with reciprocal vectors $\vec{b}_1$ and $\vec{b}_2$ defined and Miller indices assigned.

(c) Real space crystal lattice with real space vectors $\vec{a}_1$ and $\vec{a}_2$ and superdisks of fixed orientation.

Figure 4.8: Rhombic lattice assigned to SAXS pattern recorded from the middle of the sediment of capillary 3. Reflections in 4.8b and corresponding lattice planes in 4.8c have the same colour.

Figure 4.8 shows how a rhombic structure can be assigned to the SAXS pattern recorded from the middle of the sediment of sample 3. The cross shaped from factor and clear structure peaks indicate in the two dimensions perpendicular to beam a crystalline lattice of cubes with fixed orientation. Like the hexagonal pattern, the structure factor can be described by two reciprocal lattice vectors, $\vec{b}_1$ and $\vec{b}_2$, of equal length, as drawn in figure 4.8b. However, the angle between the reciprocal lattice vectors is not 60 degrees. Therefore, the two dimensional crystal structure is not hexagonal but rhombic. The rhombic structure with the cubes oriented in the direction that would give rise to the form factor of figure 4.8a is shown in 4.8c.
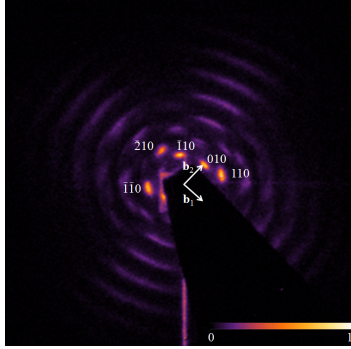
Figure 4.9: SAXS pattern recorded from the middle of the sediment of sample 4.

We are still not sure how to interpret the SAXS pattern displayed in figure 4.9. For sure, the orientation of the cubes is fixed and certainly two-dimensional long range order is present. The pattern could be interpreted as caused by a rhombic Bravais lattice, just like the SAXS pattern in figure 4.8a. In accord with this interpretation, reciprocal lattice vectors can be defined and Miller indices can be assigned as shown in figure 4.9. However, the prescence of the 010 and $\bar{2}10$ reflections is puzzling. Are the reflections visible due to a stacking feature? Or due to overlap with a form factor maximum? Why is there no $\bar{1}00$ peak visible? Is the pattern maybe caused by several crystal domains? Perhaps quantitative analysis of the pattern can answer these questions.

4.3.4 Double Rhombic

The SAXS pattern shown in figure 4.10a can be explained by the prescence of two rhombic crystal domains within the sediment irradiated with X-rays. The eight brightest reflections can be recognised as two sets of four reflections. The two sets, coloured orange and blue, discerned in figure 4.10b. Each set can be assigned to a rhombic lattice, as explained in figure 4.8. Figure 4.10c shows two real space superdisk lattices that can cause the reflections. The orientations of the cubes in the "orange" and "blue" domains are quite alike. The prescence of two crystal orientations above the height in the sediment at which single rhomic crystal domains are found can be explained by a lower osmotic pressure, that results in larege free volume for the cubes, in this part of the sediment.

(a) SAXS pattern recorded above the middle of the sediment of sample 4.

(b) Brightest reflections from 4.10a with two sets of reciprocal vectors $\vec{b}_1$ and $\vec{b}_2$ defined and Miller indices assigned.

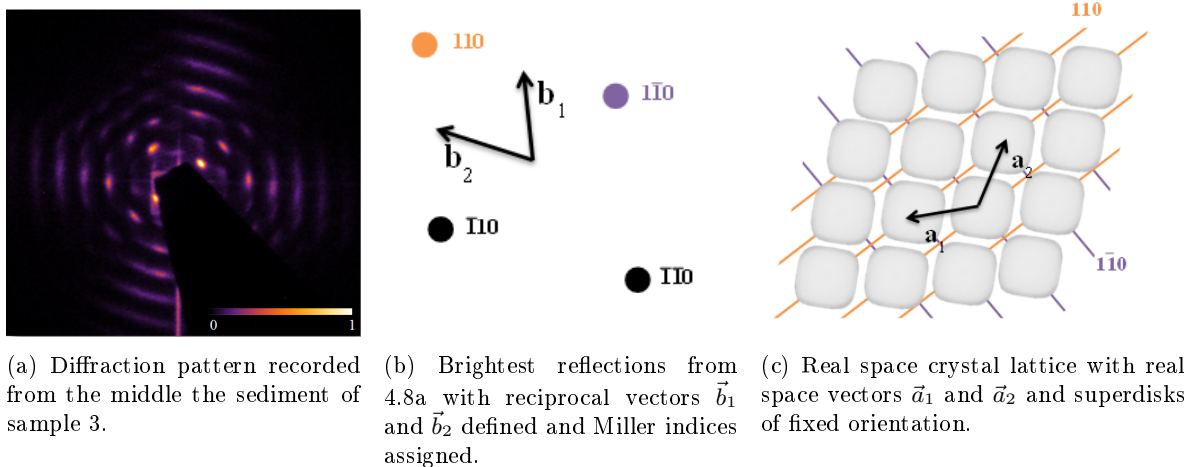(c) Two rhombic lattices described by two sets of real space vectors $\vec{a}_1$ and $\vec{a}_2$ and superdisks in two orientations.
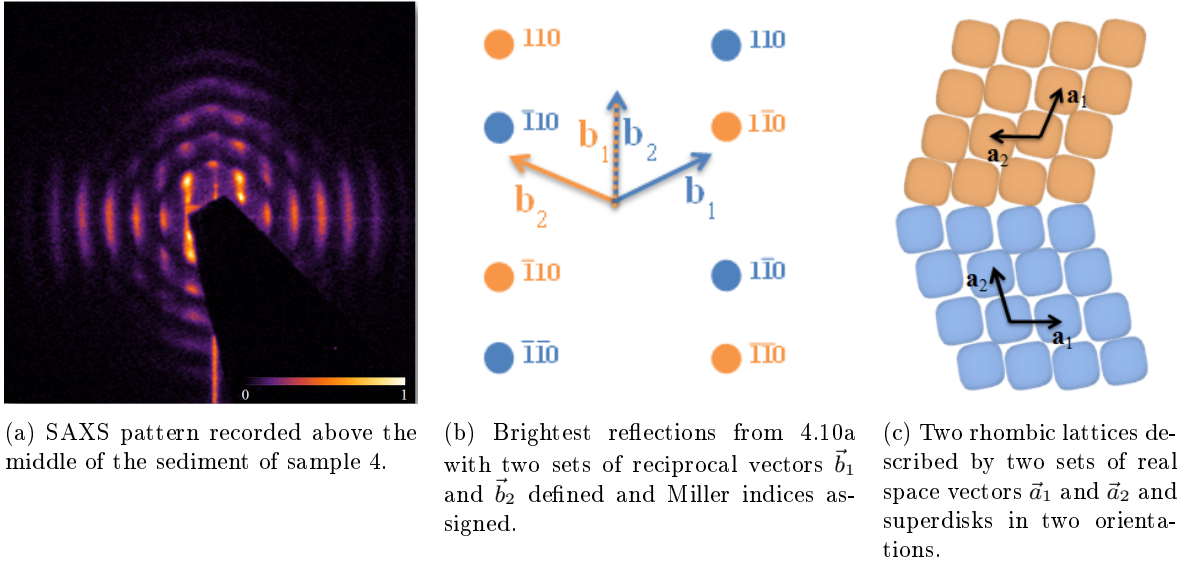
Figure 4.10: Rhombic lattice assigned to pattern recorded from the middle of the sediment of capillary 3. Reflections in 4.8b and corresponding lattice planes in 4.8c are displayed in the same colour.

4.3.5 Unresolved Structure
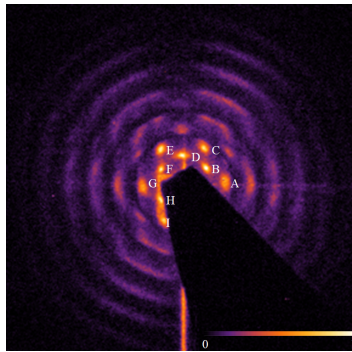
Figure 4.11: SAXS pattern recorded below the middle of the sediment of sample 4. Bragg reflections are labeled A to I.

As stated in the heading of this subsection, the pattern shown in figure 4.11 is still unresolved. The patterns shows an anisotropic form factor of threefold symmetry. Cubes oriented with their space diagonal in the direction of the beam could give rise to this form factor. Figure 4.12 provides an illustration of this orientation. Three crystal domains of cubes orientated 120° relative to each other could explain the observed form factor as well.

Figure 4.12: Threefold symmetry of a cube with rounded edges oriented with it's space diagonal pointing in the direction of the beam.

The nine structure factor peaks labeled with letters indicate long range order. The q-values of A, C, E, G and I are approximately equal and the q-values of the four inner peaks too. We tried to measure the angles between A, C, E, G and I, but since angles measured between A, D and G deviated too much from symmetry dictated sense, we do not trust these measurements. The pattern is quite sililar to the pattern in figure 4.9. The rotation scan recorded from the same position dicussed op page 45 provides some additional infromation.

4.3.6 Influence of TMAH on Crystal Structure

Figure 4.5 shows that the patterns showing the most distinct reflections are recorded from samples 3 and 4. We observed that sediments formed in the prescense of 10^{-3} M TMAH possess more long range order than sediments formed without TMAH. Tetramethylammonium hydroxide is a salt and a stong base. Being a salt, TMAH lowers the Debye screening length and increases attraction between the cubes. Being a base, TMAH increases the negative charge on the cubes (and CNCs, if present) and increases repulsion between the cubes. Attraction can lead to aggregation and when too much NaCl was added to the sedimentation capillaries, the hollow silica cubes would aggregate. Therefore, it is the alkaline property of TMAH that makes the crystals more ordered.

4.3.7 Influence of Cellulose Nanocrystals on Crystal Stucture

As can be seen in figure 4.5, the patterns recorded from the sedimentation capillaries with and without CNCs are much alike. Only for the pattern recorded from sample 4 and described in subsection 4.3.5 no counterpart was found in sample 3. But, since we do not know what cyrstal structure caused this pattern we cannot conclude anything about the influence of the CNCs from this specific pattern. In order to test if the CNCs influence the lattice spacing of the crystal, a quick comparison was made of the q-values of corresponding peaks in the "rhombic" and "double rhombic" patterns recorded from sample 3 and 4. No systematic differences in q-values were observed. The depletion interaction due to the concentration CNCs used in the experiment, as estimated on page 60, might be too low to influence the structures formed.

4.3.8 Rotation Scans

In this subsection the results of two rotation scans are discussed. The scans were made at different heights in sample 4. The upper scan was recorded 2 mm from the bottom of the capillary and the lower scan 0.7 mm. The sediment had a height of about 2.2 mm.

Upper Scan

Figure 4.13 shows the patterns obtained at certain rotation angles, ω, from the upper scan. The zero of ω is defined as the angle at wich the flat faces of the capillary were oriented approximately perpendicular to the beam.
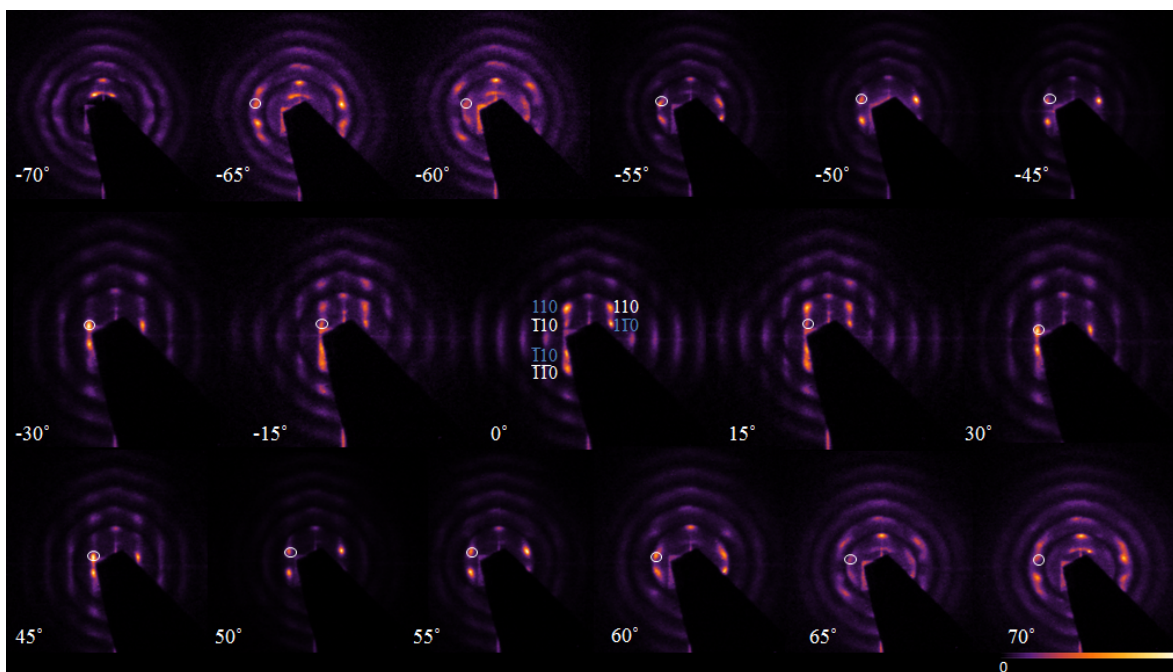

Figure 4.13: Sample 4, upper scan: SAXS patterns obtained at several rotation angles. Miller indices are assigned to the brightest peaks in the pattern recorded at an ω of 0. In the other patterns, white circles indicate the $\bar{1}10$ peak of which the x position is depicted in figure 4.14.

The SAXS pattern recorded at $\omega = 0$ is is very similar to the pattern discussed on page 42. Therefore, it can be interpreted as a pattern caused by two rhombic crystal domains with different orientations.

There are no 100 and 010 reflections visible in the patterns. These absences may be caused by bridge stacking of the layers, described in subsection 2.2.7 or by overlap with a form factor minimum.

The intensity of the $\bar{1}10$ and $1\bar{1}0$ reflections increases initially and decreases subsequently with increasing absolute value of ω. The intensities in figure 4.13 are normalised, but the intensity modulation is also visible in the raw data. Higher intensity can be interpreted as caused by an increment in order in the plane perpendicular to the direction of observation. When a crystal of periodically stacked layers is rotated, there are certain angles at which certain lattice planes are perpendicular to the direction

of observation. Therefore, the intensity modulation is an indication for periodic stacking. However, the modulation occurs over a broad range of rotation angles, so the periodicity between layers is not as regular as the periodicity within the layers.

Another feature that can be observed in the scans is that, with increasing ω, the 110, $\overline{11}0$, $\overline{1}10$ and $1\overline{1}0$ peaks move away from the center in horizontal direction. The 110 reflections and $\overline{11}0$ reflection dissapper at an rotation angle of about $|45^o|$ and reappear at $|60^o|$. That is because the peaks move into a form factor minimum. The movement of the $\overline{1}10$ reflection, indicated with the white circles in figure 4.13, is shown in graph 4.14.

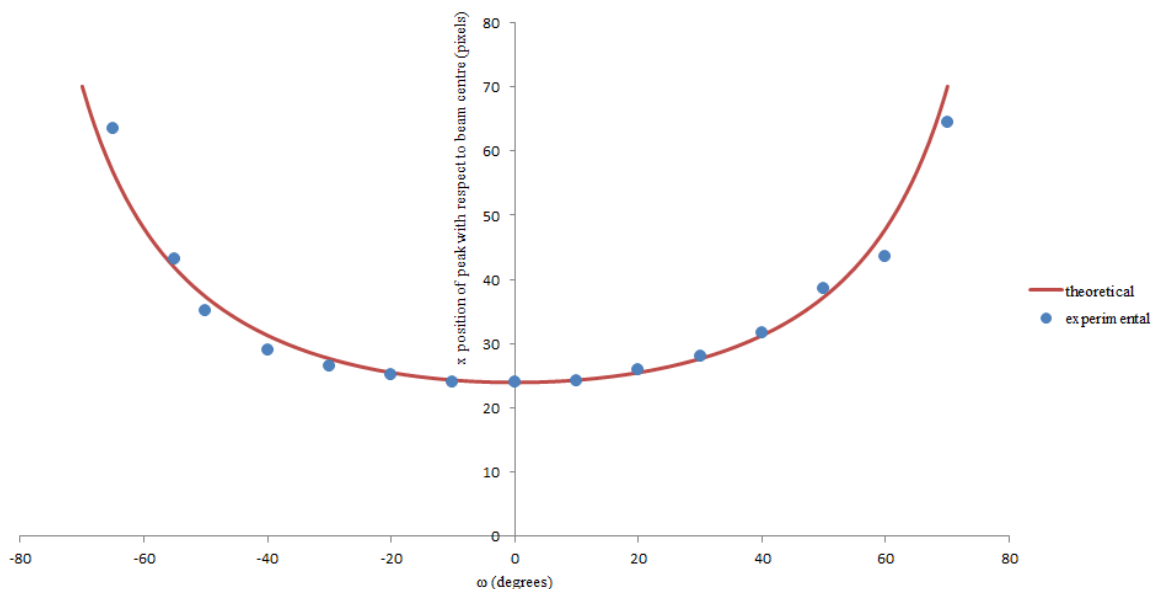Figure 4.14: Sample 4, upper scan: horizontal position of the $\overline{1}10$ reflection as function of rotation angle.

The sampled horizontal positions of the $\overline{1}10$ reflection in blue are in very good agreement with the red line. The red line shows the theoretical horizontal position as function of ω of this reflection caused by sliding phases, as described on page 22.

All in all, we find in this rotation scan one indication for bridge site stacking, one general indication for approximately periodic stacking and one indication for the prescence of sliding planes. We suggest that there is some brigde site stacking of the layers, but that there is no truely consequent stacking of the layers at the height at which this scan was recorded. More analysis of the effect of the form factor and the intensity modulations of the structure factor could give more clues to uncover the 3D structure of the crystal.

Lower Scan

Figure 4.15 shows the patterns obtained at certain rotation angles, ω, from the lower scan. The crystal structure that gave rise to the SAXS pattern recorded at $\omega = 0$ is from the same mysterious part of the crystal as the pattern described on page 42. Even with extra information from the rotation scan,

45

we do not know this structure yet. In the following, some possible interpretations of the patterns are discussed.
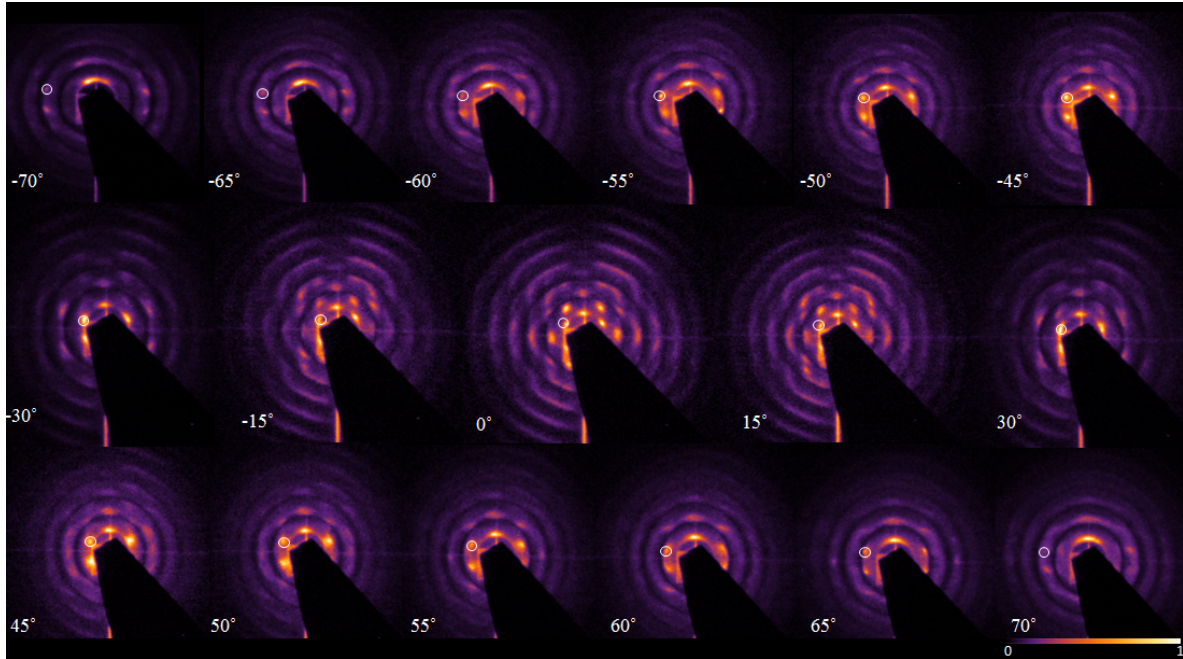
Figure 4.15: Sample 4, lower scan: SAXS patterns obtained at several rotation angles. White circles indicate the peak of which the x position is depicted in figure 4.16.

Just as for the upper scan, the horizontal movement of the peak marked by the white circle was followed as fuction of the rotation angle. The result, shown in figure 4.16, resembles the horizontal movement of the $\vec{q}$ of a Bragg rod as function of ω very much. This indicates the prescence of sliding planes. However, the threefold symmetry of the form factor in the pattern recorded at $\omega = 0$ may be caused by cubes pointing with their space diagonal in the direction perpendicular to the flat faced of the capillary, see figure 4.12. Cubes oriented in that direction logically cannot form sliding planes. The other explanation for the threefold symmetry of the structure factor mentioned was the prescence of three differently orented rhombic lattices. That contrasts to the observation that "double rhombic" patterns were recorded from higher positions than single rhombic patterns. All in all, a comprehensive interpretation of this scan is still missing.

Figure 4.16: Sample 4, lower scan: horizontal position of the reflection indicated by the white circle in figure 4.15 as function of rotation angle.
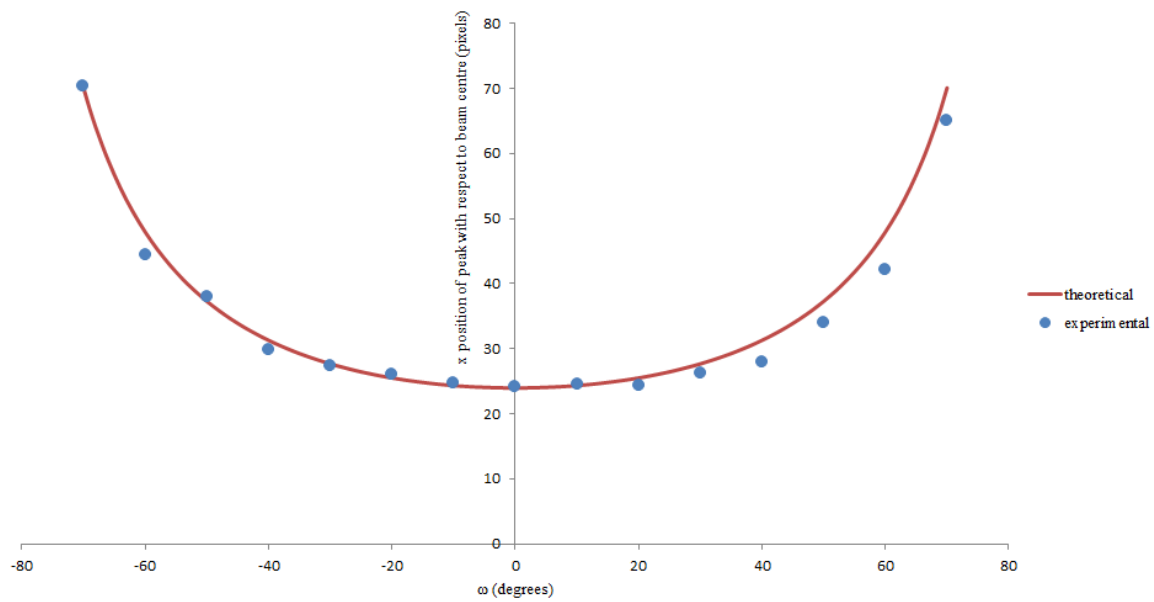
Chapter 5

Conclusions

Cellulose nanocrystals (CNCs) and fluorescently labeled CNCs were prepared via acid hydrolysis of cotton paper. Using transmission electron microscopy (TEM), the length of the nonfluorescent CNCs was determined to be $0.44 \pm 0.03\,\mu$m. Hollow silica cubes (HSCs) were characterized by TEM and a superdisk shape was fitted to the TEM pictures. The edgelength of the HSCs was $1.046 \pm 0.007\,\mu$m, their m-value 3.5287 ± 0.0068 and the aspect ratio between the two edgelengths 1.0042 ± 0.0030.

Concentration series of mixtures of CNCs and dextran 70 were prepared. Microscopy with crossed polarizers showed formation of cholesteric tactiods within the isotropic phase of samples with a CNC concentration of 5.0 wt% and a dextran concentration between 0.0 and 1.8 wt% dextran and a sample with a CNC concentration of 4.5 wt% a dextran concentration of 1.4 wt%. Tactoid formation and growth was observed to take place on timescales of weeks and months.

Small angle X-ray scattering (SAXS) studies have shown the presence of sedimentation induced layered crystals of HSCs in capillaries with flat walls. Similar SAXS patterns were recorded from HSC crystals formed in prescence and absence of CNCs. Theoretical superdisk form factors were recognized in the patterns and were used to determine particle orientation. Structure factors of hexagonal and rhombic two-dimensionals crystal lattices were identified as well. From the top to the bottom of the sediments, rotator hexagonal phases, bi-domain rhombic phases, single domain rhombic phases and unordered phases could be identified. Rotation scans indicated prescence of bridge site stacking and random stacking of the rhombic lattices in the bi-domain rhombic region.

The presense of rotator hexagonal phases at the top of the sediment and rhombic phases lower in the sediment is in good agreement with results from simulations perfomed by Avedaño et al. [17]. The rhombic crystal lattice can be identified as the dense packed Λ_1 superdisk lattice predicted by Jiao et al. [16]. All identified crystal structures equal structures found by Janne-Mieke Meijer [10] in sedimentation induced HSC crystals in absence of depletants. The Λ_1 phase was also found in depletion induced HSC crystals with polymer depletants by Rossi et al. [9]. All in all, more research is needed to conclude on the influence of CNCs on HSC crystallization.

Chapter 6

Outlook

Since this thesis comprises research on two distinct topics, the outlook is divided into two sections.

6.1 Regarding the Spherically Confined Cholesteric of CNCs

The CNCs described in this thesis should be characterized better when used in future experiments. Their diameters remain unknown and the fluorescently labeled ones are not characterized at all. Good AFM measurements would be a superior source of information.

Systems containing cholesteric tactoids of CNCs could be optimized further by analysis of tactoid abundancy and pitch lenth as function of CNC and dextran concentration. Experiments described in this thesis should be reproduced, other depletants could be used and fluorescently labeled CNCs and depletants could be utilized to clarify the influence of depletion interaction on the formation of cholesteric tactoids.

Nevertheless, the tactoid containing systems described in this thesis are far from being researched sufficiently. Lyotropic nematic tactoids have been studied and their shapes can be explained and used to derive interesting material parameters. [56] [57] [58] [59] [60] [61] [62] [63] However, tactoids of chiral nematic phases do not seem to be investigated systematically. In line of the work described in [61], tactoid shapes could be analysed, experiments with external fields could be performed and droplet coalescence could be studied. Yet, some theorizing and computer simulating should be performed beforehand and long timescales must be taken into account.

Although it was not accomplished during the beam trip described in this thesis, it certrainly is possible to investigate CNCs [6] and their cholesteric phase [64] using SAXS. Therefore, it would be a good idea to try to achieve scattering signal from the depletion series using another SAXS set-up. Perhaps better data correction, SAXS dedicated equipment, a less intense X-ray beam, longer exposure times or larger sample volumes could improve the signal. Small angle neutron scattering can be used to study the CNC cholesteric [65] and may also be an interesting technique to research the tactoids.

Besides tactoids, other means of confinement of the cholesteric of CNCs may be interesting as well. Pilot attempts were made to confine CNCs dispersed in a hydrophilic phase in droplets within an

hydrophobic phase. No stable emulsions were obtained, but it could be interesting to try again or use other solvents.

6.2   Regarding Crystallization of HSCs in presence of CNCs

The vast majority of the SAXS patterns recorded from the sedimentation samples described in this thesis is still waiting to be analysed. Quantitative analysis of the q-values and calculation of the lattice spacings would be very interesting. One of the reasons to perform quantitative analysis would be that it could lead to full understanding of the structures giving rise to patterns such as figure 4.9 and 4.11. Another reason is that quantitative analysis is needed to compare the structures formed in the different sedimentation samples described in this thesis. Bragg rod analysis, such as performed in [43], may provide comprehensive information on the stacking of layers.

To investigate the influence of CNCs on the crystallization of HSCs, higher CNCs concentrations, providing stronger depletion interactions, would be interesting. Moreover, CNCs could be compared to other depletants. Results of experiments with polyethylene oxide are still waiting to be analysed. Microscopy studies, like performed by Laura Rossi et al. [8], can be performed to find out whether CNCs can induce crystallization of hollow silica cubes under circumstances that would not lead to crystallization without depletants. Perhaps it would be interesting to induce crystallization using convective assembly in mixtures of cellulose nanocrystals and hollow silica cubes.

Chapter 7

Acknowledgements

First of all, I would like to say thanks to Jasper. Actually, I wanted to thank you with a Douglas Adams quote, but I only could find something with fish. So, I'll just thank you for helping me with everything, explaining me so much and always being available for questions. Thank you for the LaTeXtemplates and Mathematica scripts that make life more easy. I really enjoyed working with you and I am looking foreward to the next beam trip. Andrei, I would like to thank you for your enthousiasm in showing the ESRF, for the good advices and for the times you would just walk into the bachelor room to explain me something I needed to know about scattering.

Samia, thank you too for being good company at the ESRF and for the TEM sessions. I would like to thank Janne-Mieke for having written a very helpful thesis and explaining me how to analyse SAXS data. Burak, although none of the experiments with the emulsions and the organogels made it to this thesis, I learned a lot from them. Without Mark three weeks of work I did not back-up would have been lost. Yong is thanked for the TEM sessions and his help with iTEM. Rumen, thank you for helping me with the presentation and just for the conversations. Thanks, Bonny, for the help with electrical devices and arranging the AFM session, even though it is not mentioned in this thesis. Lennert is thanked for his help with the AFM and Gavin for the X-ray set-ups. Maarten, thank you for reading the thesis and correcting typos and vague language.

Finally, I would like to thank the Crystal Club for advice and FCC for it's friendly atmosphere (and friday cookies).

Bibliography

[1] H. N. W. Lekkerkerker and R. Tuinier, *Colloids and the Depletion Interaction.* Springer, 2011.

[2] A. K. Mohantya, M. Misraa, and G. Hinrichsen, "Biofibres, biodegradable polymers and bio-composites: An overview," *Macromolecular materials and engineering*, vol. 276/277, pp. 1–24, 2000.

[3] S. J. Eichhorn, "Cellulose nanowhiskers: promising materials for advanced applications," *Soft Matter*, vol. 7, no. 2, p. 303, 2011.

[4] M. Jarvis, "Chemistry: Cellulose stacks up," *Nature*, vol. 426, pp. 611–612, 2003.

[5] B. G. Ranby, "The colloidal properties," *Discussions of the Faraday Society*, vol. 11, no. 1, pp. 158–164, 1951.

[6] S. Elazzouzi-Hafraoui, Y. Nishiyama, J. L. Putaux, L. Heux, F. Dubreuil, and C. Rochas, "The shape and size distribution of crystalline nanoparticles prepared by acid hydrolysis of native cellulose," *Biomacromolecules*, vol. 9, no. 1, pp. 57–65, 2008.

[7] J. F. Revol, H. Bradford, J. Giasson, R. H. Marchessault, and D. G. Gray, "Helicoidal self-ordering of cellulose microfibrils in aqueous suspension.," *International journal of biological macromolecules*, vol. 14, no. 3, pp. 170–172, 1992.

[8] L. Rossi, S. Sacanna, W. T. M. Irvine, P. M. Chaikin, D. J. Pine, and A. P. Philipse, "Cubic crystals from cubic colloids," *Soft Matter*, vol. 7, no. 9, p. 4139, 2011.

[9] L. Rossi, V. Soni, D. J. Ashton, D. J. Pine, A. P. Philipse, P. M. Chaikin, M. Dijkstra, S. Sacanna, and W. T. M. Irvine, "Shape-sensitive crystallization in colloidal superball fluids," *Proceedings of the National Academy of Sciences*, vol. 112, no. 12, pp. 5286–5290, 2015.

[10] J.-M. Meijer, *Colloidal Crystals of Spheres and Cubes in Real and Reciprocal Space.* PhD thesis, Utrecht University, Utrecht, 2015.

[11] Y. Jiao, F. H. Stillinger, and S. Torquato, "Optimal packings of superballs," *Statistical, Nonlinear, and Soft Matter Physics*, vol. 79, no. 4, pp. 1–12, 2009.

[12] R. D. Batten, F. H. Stillinger, and S. Torquato, "Phase behavior of colloidal superballs: Shape interpolation from spheres to cubes," *Physical Review E - Statistical, Nonlinear, and Soft Matter Physics*, vol. 81, no. 6, pp. 1–13, 2010.

[13] R. Ni, A. P. Gantapara, J. de Graaf, R. van Roij, and M. Dijkstra, "Phase diagram of colloidal hard superballs: from cubes via spheres to octahedra," *Soft Matter*, vol. 8, no. 34, p. 8826, 2012.

[14] Y. Zhang, F. Lu, D. Van Der Lelie, and O. Gang, "Continuous phase transformation in nanocube assemblies," *Physical Review Letters*, vol. 107, no. 13, pp. 2–5, 2011.

[15] H. J. Yang, S. Y. He, H. L. Chen, and H. Y. Tuan, "Monodisperse copper nanocubes: synthesis, self-assembly, and large-area dense-packed films," *Chemistry of Materials*, vol. 26, no. 5, pp. 1785–1793, 2014.

[16] Y. Jiao, F. H. Stillinger, and S. Torquato, "Optimal packings of superdisks and the role of symmetry," *Physical Review Letters*, vol. 100, no. 24, pp. 2–5, 2008.

[17] C. Avendaño and F. a. Escobedo, "Phase behavior of rounded hard-squares," *Soft Matter*, vol. 8, no. 17, p. 4675, 2012.

[18] L. Kroon-Batenburg, *Kristallografie dictaat*. Utrecht University, 3rd editio ed., 2013.

[19] A. V. Petukhov and G. J. Vroege, *Advanced (Super)structures, Scattering & Microscopy: dictaat scattering*. Utrecht University.

[20] C. D. Edgar and D. G. Gray, "Influence of dextran on the phase behavior of suspensions of cellulose nanocrystals," *Macromolecules*, vol. 35, no. 19, pp. 7400–7406, 2002.

[21] J. Landman, *Controlled evaporation and optical properties of colourful chiral nematic cellulose films*. PhD thesis, University of Cambridge, 2013.

[22] A. R. Barron and C. Xiang, *Physical methods in chemistry and nano science*. OpenStax-CNX, 2015.

[23] R. H. Marchessault, F. F. Morehead, and N. M. Walter, "Liquid crystal systems from fibrillar polysaccharides," *Nature*, vol. 184, pp. 632 − 633, 1959.

[24] X. Dong, "Effect of microcrystallite preparation conditions on the formation of colloid crystals of cellulose," *Water*, vol. 5, no. 1, pp. 19–32, 1998.

[25] S. Beck-Candanedo, M. Roman, and D. G. Gray, "Effect of reaction conditions on the properties and behavior of wood cellulose nanocrystal suspensions," *Biomacromolecules*, vol. 6, no. 2, pp. 1048–1054, 2005.

[26] S. Beck-Candanedo, D. Viet, and D. G. Gray, "Induced phase separation in low-ionic-strength cellulose nanocrystal suspensions containing high-molecular-weight blue dextrans," *Langmuir*, vol. 22, no. 21, pp. 8690–8695, 2006.

[27] S. Beck-Candanedo, D. Viet, and D. G. Gray, "Induced phase separation in cellulose nanocrystal suspensions containing ionic dye species," *Cellulose*, vol. 13, no. 6, pp. 629–635, 2006.

[28] S. Beck-Candanedo, D. Viet, and D. G. Gray, "Triphase equilibria in cellulose nanocrystal suspensions containing neutral and charged macromolecules," *Macromolecules*, vol. 40, no. 9, pp. 3429–3436, 2007.

[29] A. Hirai, O. Inui, F. Horii, and M. Tsuji, "Phase separation behavior in aqueous suspensions of bacterial cellulose nanocrystals prepared by sulfuric acid treatment.," *Langmuir*, vol. 25, no. 1, pp. 497–502, 2009.

[30] E. E. Ureña Benavides, G. Ao, V. A. Davis, and C. L. Kitchens, "Rheology and phase behavior of lyotropic cellulose nanocrystal suspensions," *Macromolecules*, vol. 44, no. 22, pp. 8990–8998, 2011.

[31] W. J. Orts, L. Godbout, R. H. Marchessault, and J.-F. Revol, "Enhanced ordering of liquid crystalline suspensions of cellulose microfibrils: a small angle neutron scattering study," *Macromolecules*, vol. 31, no. 17, pp. 5717–5725, 1998.

[32] Y. Habibi, L. a. Lucia, and O. J. Rojas, "Cellulose Nanocrystals : Chemistry , Self-Assembly , and Applications," *Chemical reviews*, vol. 110, pp. 3479–3500, 2010.

[33] M. M. De Souza Lima and R. Borsali, "Rodlike cellulose microcrystals: structure, properties, and applications," *Macromolecular Rapid Communications*, vol. 25, no. 7, pp. 771–787, 2004.

[34] B. Holt, S. Stoyanov, E. Pelan, and V. Paunov, "Novel anisotropic materials from functionalised colloidal cellulose and cellulose derivatives," *Journal of Materials Chemistry*, vol. 20, pp. 10058–10070, 2010.

[35] C. E. Ioan, T. Aberle, and W. Burchard, "Structure properties of dextran. 2. Dilute solution," *Macromolecules*, vol. 33, no. 15, pp. 5730–5739, 2000.

[36] L. Rossi, S. Sacanna, W. T. M. Irvine, P. M. Chaikin, D. J. Pine, and A. P. Philipse, "Cubic crystals from cubic colloids," *Soft Matter*, vol. 7, no. 9, p. 4139, 2011.

[37] A. P. Philipse and G. H. Koenderink, "Sedimentation-diffusion profiles and layered sedimentation of charged colloids at low ionic strength," *Advances in Colloid and Interface Science*, vol. 100-102, pp. 613–639, 2003.

[38] G. B. Alexander, W. M. Heston, and R. K. Iler, "The solubility of amorphous silica in water," *Journal of Physical Chemistry*, vol. 6, no. 58, pp. 453–455, 1954.

[39] G. Milkereit, M. Morr, J. Thiem, and V. Vill, "Thermotropic and lyotropic properties of long chain alkyl glycopyranosides: Part III: pH-sensitive headgroups," *Chemistry and Physics of Lipids*, vol. 127, no. 1, pp. 47–63, 2004.

[40] L. Onsager, "The effects of shape on the interaction of colloidal particles," *Annals of the New York Academy of Sciences*, vol. 51, no. 4, pp. 627–659, 1949.

[41] D. Frenkel, "Perspective on "The effect of shape on the interaction of colloidal particles"," *Theoretical Chemistry Accounts*, vol. 103, pp. 212–213, 2000.

[42] M. A. van Huis and H. Friedrich, "7 Electron Microscopy Techniques,"

[43] A. Pal, J.-M. Meijer, J. R. Wolters, W. K. Kegel, and A. V. Petukhov, "Structure and stacking order in crystals of asymmetric dumbbell-like colloids," *Journal of Applied Crystallography*, vol. 48, no. 1, pp. 238–243, 2015.

[44] Sigma Aldrich, "Blue Dextran Info Sheet."

[45] T. Sugimoto, K. Sakata, and A. Muramatsu, "Formation Mechanism of Monodisperse Pseudocubic a-Fe2o3 particles from condensed ferri hydroxide gel," *Journal of Colloid and Interface Science*, vol. 159, pp. 372–382, 1993.

[46] V. Meester, *Self-assembly of micron-sized hollow silica cubes using convective assembly methods.* PhD thesis, Utrecht University, 2014.

[47] S. I. Castillo, S. Ouhajji, S. Fokker, B. H. Erné, C. T. Schneijdenberg, D. M. Thies-Weesie, and A. P. Philipse, "Silica cubes with tunable coating thickness and porosity: From hematite filled silica boxes to hollow silica bubbles," *Microporous and Mesoporous Materials*, vol. 195, pp. 75–86, 2014.

[48] ESRF, "ID11 - Materials science beamline."

[49] S. S. R. Facility, "Detectors."

[50] SPIE, "Refractive lenses allow compact, precision focusing of x-rays."

[51] University of Nebraska-Lincoln, "Next Generations of X-ray Lightsource."

[52] J.-M. Meijer, "Personal correspondence,"

[53] B. R. Pauw, "Corrigendum: Everything SAXS: small-angle scattering pattern collection and correction (2013 J. Phys.: Condens. Matter 25 383201)," *Journal of Physics: Condensed Matter*, vol. 26, no. 23, p. 239501, 2014.

[54] D. Liu, X. Chen, Y. Yue, M. Chen, and Q. Wu, "Structure and rheology of nanocrystalline cellulose," *Carbohydrate Polymers*, vol. 84, no. 1, pp. 316–322, 2011.

[55] T. Sugimoto and K. Sakata, "Preparation of monodisperse pseudocubic alpha-Fe2O3 particles from condensed ferric hydroxide gel," *Journal of Colloid and Interface ScienceInterface*, vol. 152, no. 2, pp. 587–590, 1992.

[56] A. V. Kaznacheev, M. M. Bogdanov, and S. A. Taraskin, "The nature of prolate shape of tactoids in lyotropic inorganic liquid crystals," *Journal of Experimental and Theoretical Physics*, vol. 95, no. 1, pp. 57–63, 2002.

[57] A. V. Kaznacheev, M. M. Bogdanov, and A. S. Sonin, "The influence of anchoring energy on the prolate shape of tactoids in lyotropic inorganic liquid crystals," *Journal of Experimental and Theoretical Physics*, vol. 97, no. 6, pp. 1159–1167, 2003.

[58] P. Prinsen and P. van der Schoot, "Shape and director-field transformation of tactoids.," *Statistical, nonlinear, and soft matter physics*, vol. 68, pp. 1–11, 2003.

[59] M. A. Bates, "Computer simulation studies of nematic liquid crystal tactoids," *Chemical physics letters*, vol. 368, pp. 87–93, 2003.

[60] P. Prinsen and P. Van Der Schoot, "Continuous director-field transformation of nematic tactoids," *European Physical Journal*, vol. 13, no. 1, pp. 35–41, 2004.

[61] L. Verhoeff, *Liquid crystal drops in suspensions of colloidal platelets*. Phd thesis, Utrecht University, 2011.

[62] L. F. Rull, J. M. Romero-Enrique, and a. Fernandez-Nieves, "Computer simulations of nematic drops: Coupling between drop shape and nematic order," *Journal of Chemical Physics*, vol. 137, no. 3, 2012.

[63] D. Vanzo, M. Ricci, R. Berardi, and C. Zannoni, "Shape, chirality and internal order of freely suspended nematic nanodroplets," *Soft Matter*, vol. 8, no. 47, pp. 11790–11800, 2012.

[64] C. Schütz, M. Agthe, A. B. Fall, K. Gordeyeva, V. Guccini, M. Salajková, T. S. Plivelic, J. P. F. Lagerwall, G. Salazar-Alvarez, and L. Bergström, "Rod packing in chiral nematic cellulose nanocrystal dispersions studied by small-angle X-ray scattering and laser diffraction," *Langmuir*, vol. 31, pp. 6507–6513, 2015.

[65] W. J. Orts, L. Godbout, R. H. Marchessault, and J.-F. Revol, "Enhanced ordering of liquid crystalline suspensions of cellulose microfibrils: s small angle neutron scattering study," *Macromolecules*, vol. 31, no. 17, pp. 5717–5725, 1998.

[66] WolframMathworld, "Horizontal cylindrical segment."

[67] C. Osuji, "Radius of Gyration," *Polymer physics, lecture notes*, 2013.

Chapter 8

Appendices

These appendices comprise simple calculations in real and reciprocal space and a list of the symbols used in this thesis.

8.1 Real Space

In this section, Debye screening lengths are calculated for systems containing hollow silica cubes and gravitational lengths and depletion potentials are estimated for models of both sytems described in this thesis.

8.1.1 Calculation of Debye Screening Length for Sedimentation Capillaries 1 and 3

The Debye screening length, κ^{-1} can be calculated using:

$$\kappa^{-1} = \sqrt{\frac{\epsilon_0 \epsilon_r kT}{2N_A e^2 I}}$$

For the permittivity of vacuum, ϵ_0, a value of 8.85 Fm^{-1} is used, for ϵ_r, the dielectric constant of the solvent, 80.4 is used. Values of 1.38 x 10^{-23} m^2 $kgms^{-2}K^{-1}$ for the Boltzmann constant, k, 300 K for the temperature, T, 6.02 x 10^{23} mol^{-1} for Avogadro's constant, N_A, and 1.60 x 10^{-19} C for the elementary charge, e, are used. I, the ionic strength of the solution can be calculated with:

$$I = \frac{1}{2} \sum_{i=1}^{n} c_i z_i^2$$

where c_i is the concentration of ion i and z_i its charge number. Both NaCl and TMAH are 1:1 salts

and the ionic strength is just the total salt concentration.

The Debye screening length in a solution of 1.0 x 10^{-4} M NaCl, like in sedimentation capillary 1, 30 nm. If, like in sample 3, 1 x 10^{-3} M TMAH is present as well, κ^{-1} is 9 nm.

8.1.2 Calculation of the Gravitational Length for Simple Models of the Colloids

The gravitational length, L_{g}, can be calculated using:

$$L_{\mathrm{g}} = \frac{kT}{\Delta mg}$$

For the Boltzmann constant, k, a value of 1.38 x 10^{-23} m^2 kgms^{-2}K^{-1} is used, for the gravitational acceleration 9.81 ms^{-2} and for the temperature, T, 300 K. The density of the solvent is assumed to be 1 gcm^{-3}.

The cellulose nanocrystals are modelled as cylinders with a length of 440 nm and a radius of 5 nm. When 1.5 gcm^{-3} is used for the density, Δm is 1.73 x 10^{-20} kg and the cylinders have a gravitational length of 2.4 cm.

As a model for the hollow silica cubes, perfect cubes with an edgelength of 1000 nm and a silica layer thickness of 100 nm are used. Using 1.6 gcm^{-3} for the density of silica, Δm is 1.63 x 10^{-16} kg, which leads to a gravitational length of 2.6 µm.

8.1.3 Order of Magnitude Estimates of Depletion Interaction

In this subsection Asakura-Oosawa-Vrij (AOV) depletion potentials are calculated for a system of colloidal cylinders in the prescence of ideal polymers as a model for the CNCs with dextran in the "depletion series" and for a system of colloidal cubes in the surrouded by hard rods as a model for the hollow silica cubes and CNCs in the "sedimentation experiment". As described op page 12 the AOV depletion potential is given by:

$$W_{dep}(h) = \left\{ \begin{array}{ll} 0 & \text{if } h \geq 2\delta \\ \text{-}\Pi V_{ov}(h) & \text{if } 0 \leq h \leq 2\delta \\ \infty & \text{if h<0} \end{array} \right\}$$

with h the distance between two colloids and δ the thickness of the depletion layer. The ideal osmotic pressure, Π, of depletants can be calculated with:

$$\Pi = n_{\mathrm{b}}kT$$

where $n\$(_{\mathrm{b}}$ is the bulk number density of the depletant, k, the Boltzmann constant and T the temperature. [1]

Depletion Interaction between Cylinders due to Ideal Polymers

(a) $h \geq 2\delta$.   (b) $0 \leq h \leq 2\delta$.   (c) h=0
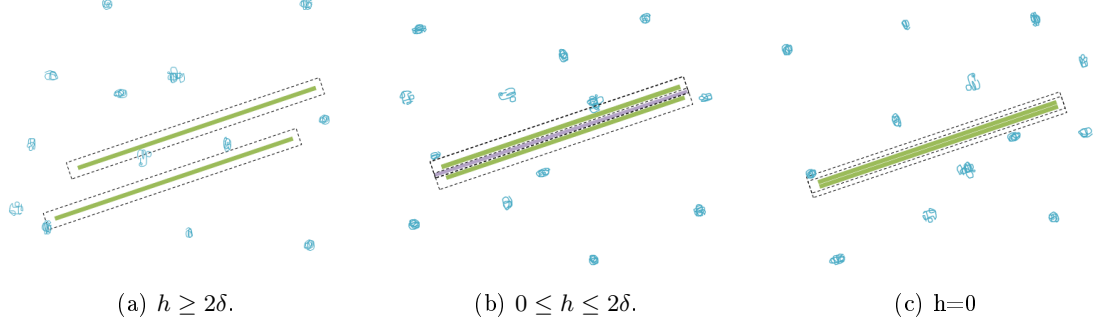
Figure 8.1: Illustration of depletion interaction between cylinders, in green, and ideal polymers, in blue. The depletion layers surrounding the cylinders are indicated with dashed lines and the overlap volume is coloured purple.

(a) Overlap Volume of Depletion Layers of two Cylinders.

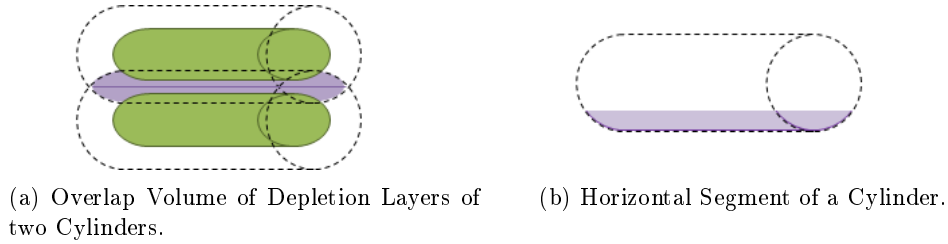(b) Horizontal Segment of a Cylinder.

Figure 8.2: Overlap volume of depletion layers of two cylinders can be calculated as twice the volume of a horizontal segment of a cylinder. Overlap volume and segment volume are marked purple.

1.5 wt% ideal polymer with a molecular mass of 70000 gmol^{-1} causes an osmotic pressure of 5.4 hPa. The thickness of the depletion layer is equal to the radius of gyration of the polymer. The overlap volume of the depletion layers in the situation depicted in figure 8.1b is illustrated more clearly in figure 8.2. Note that figures are not to scale. From the figure it may be clear that the overlap volume can be calculated as two times the volume of a horizontal segment of a cylinder. Therefore, the overlap volume, V_{ov}, can be calculated using [66]:

$$V_{\text{ov}} = 2L \left(R^2 \cos^{-1} \left(\frac{R-x}{R} \right) - (R-x)\sqrt{2Rx - x^2} \right)$$

where R is the radius of the cylinder, L it's length and x the height of the segment. When the rods have a length of 440 nm and a diameter of 10 nm and the radius of gyration of the polymer is 8 nm, the depletion layer has outer dimensions of L=456 nm and R=18 nm. When the cylinders touch (h=0), see figure 8.1b, x equals the thickness of the depletion layer, 8 nm in this calculation. The difference in energy between this situation and the situation in which the depletion volumes just touch (h=2δ) is 1.4 x 10^{-19} J, or 35 times kT.

Depletion Intercation between Cubes due to Hard Rods

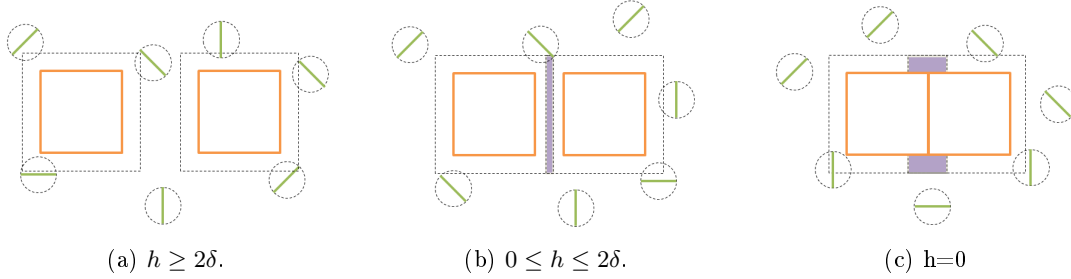(a) $h \geq 2\delta$.   (b) $0 \leq h \leq 2\delta$.   (c) h=0

Figure 8.3: Illustration of depletion interaction between cubes, in orange, and rods, in green. The dashed lines around the cubes inducate depletion layers and the dashed lines around the rods mark the spheres assumed to be occupied by the rods. The overlap volume is marked purple.

In this calculation, it is assumed that the rods can rotate freely and effectively occupy a spherical piece of space. A dispersion with a density of 1 kgL^{-1}, that contains 2 x 10^{-2} wt% rods with length 440 nm, diameter 10 nm and density 1.5 gcm^{-1} has an osmotic pressure of 16 Pa. The overlap volume is approximated as twice the area of one face of the cube times the thickness of the depletion layer. When two cubes with edge lengths of 1 μm touch (h=0), see figure 8.3c, the overlap volume is 1.6 x 10^{-20} m. Therefore, a depletion attraction of 3 x 10^{-21} J, or 0.6 kT is found.

8.1.4 Calculation of Size Ration between Superball and Depletant

Rossi et al. [9] found that the structures into which superballs crystallized in prescence of depletants depended on size ratio:

$$q = \frac{2R_{\mathrm{g}}}{D}$$

with R_{g} the radius of gyration of the depletant and D the edgelength of the superball. For cylinders, the the radius of gyration is given by:

$$R_{\mathrm{g}}^2 = \frac{R^2}{2} + \frac{L^2}{12}$$

with R the radius and L the length of the cylinder. [67] For cylinders with R= 5.0 nm and L=440 nm and superballs with D=1.0 μm, q=0.25.

8.2 Reciprocal Space

8.2.1 Notation: Scattering and Crystallography

In literature on scattering and literature on crystallography different definitions are used. The greek letter θ is used for both the scattering angle used by scatterers and the Bragg angle used by crystallographers. As can be seen in figure 8.4, the scattering angle is twice the Bragg angle. [19]
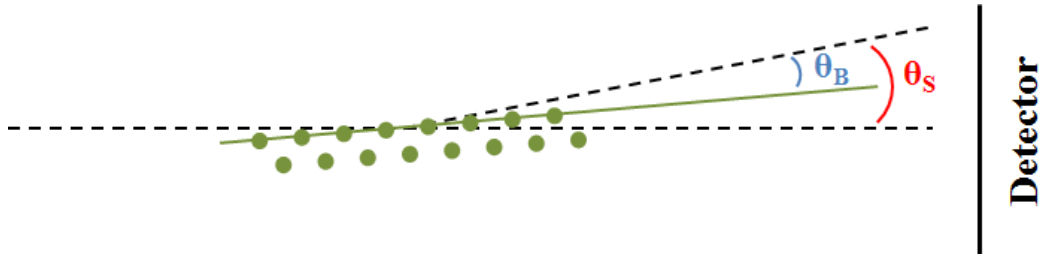

Figure 8.4: Defining the Bragg angle, θ_B, and scattering angle, θ_S. The dotted lines indicate the incoming, diffracted and not diffracted X-rays. The green spheres represent a crystal and the line through them the crystal plane that diffracts the rays.

Also the conversion from real to reciprocal space is performed differently in the two fields. When a translational lattice can be described by the axes $\vec{a}_1$, $\vec{a}_2$ and $\vec{a}_3$, crystallographers [18] tend to define the reciprocal lattice vectors as:

$$\vec{b}_1 = \frac{\vec{a}_2 \times \vec{a}_3}{V}$$

$$\vec{b}_2 = \frac{\vec{a}_3 \times \vec{a}_1}{V}$$

$$\vec{b}_3 = \frac{\vec{a}_1 \times \vec{a}_2}{V}$$

with V the volume of the real space unit cell:

$$V = \vec{a}_1 \cdot |\vec{a}_2 \times \vec{a}_3|$$

However, in scattering, these reciprocal vectors are multiplied by a factor 2π.

8.2.2 Assumption of Effect of Hollowness on Form Factor

The effect of hollowness on the form factor can be estimated for a spherical model particle. That is because the form factor of a sphere can be calculated analytically. The unnormalised form factor of a

homogeneous sphere with radius a and scattering length density ζ is [19] :

$$P(\vec{q}) = \left| \frac{4\pi}{3} a^3 \Delta\zeta \right|^2 \left(3\frac{\sin qa - qa\cos qa}{(qa)^3} \right)^2$$

The scattering amplitude of a hollow sphere is the scattering amplitude of the sphere with radius a minus the scattering amplitude of a smaller sphere with radius ηa. The scattered intensity of the hollow sphere is its scattering amplitude multiplied by its complex conjungate, or its scattering amplitude squared:

$$P(\vec{q}) = \left| \frac{4\pi}{3} a^3 \Delta\zeta \right|^2 \left[3\frac{\sin qa - qa\cos qa}{(qa)^3} - 3\eta^3\frac{\sin q\eta a - q\eta a\cos q\eta a}{(q\eta a)^3} \right]^2$$

$$= \left| \frac{4\pi}{3} a^3 \Delta\zeta \right|^2 \left[3\frac{\sin qa - qa\cos qa - \eta^3(\sin q\eta a - q\eta a\cos q\eta a)}{(qa)^3} \right]^2$$
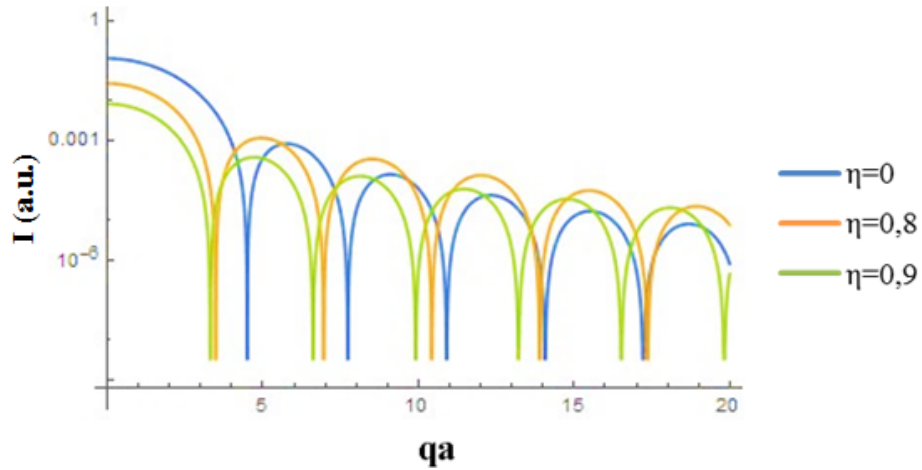

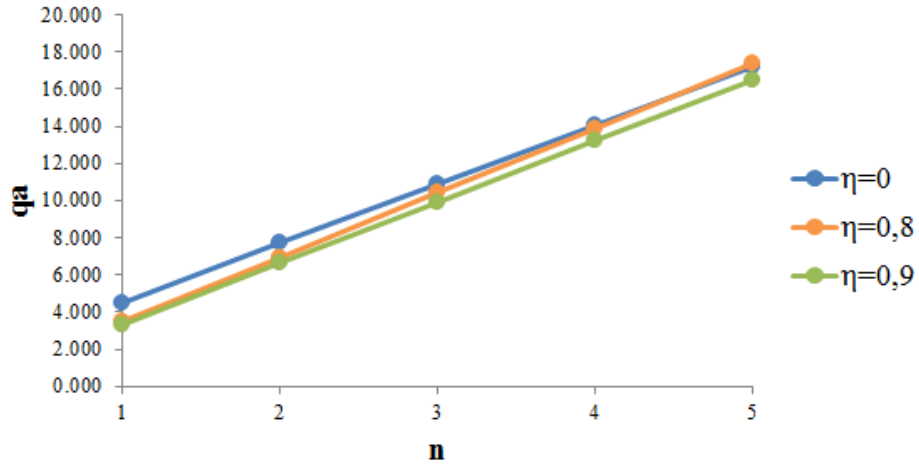Figure 8.5: Unnormalized form factor of filled ($\eta = 0$) or hollow ($\eta = 0.8$, $\eta = 0.9$) spheres.

Figure 8.6: Position of the n$^{\text{th}}$ form factor minimum for several values of η.

In figure 8.5 $\left[3\frac{\sin qa - qa\cos qa - \eta^3(\sin q\eta a - q\eta a\cos q\eta a)}{(qa)^3}\right]^2$ is plotted as function of qa for several values of η. From this figure, it is clear that with increasing hollowness, the form factor minima move to lower q-values. The positions of the form factor minima are shown in figure 8.6.

8.3 List of Symbols

a	radius of sphere
$\vec{a}_1, \vec{a}_2, \vec{a}_3$	crystal axes
$\vec{b}_1, \vec{b}_2, \vec{b}_3$	reciprocal axes
c	concentration
d_{hkl}	distance between lattice planes
g	gravitational constant
D	edgelength
δ	thickness of depletion layer
e	elementary charge
ϵ_0	permittivity of vacuum
ϵ_r	dielectric constant of solvent
ζ	scattering length density
η	ratio inner and outer radius of hollow sphere
$\theta, \theta_\mathrm{s}$	scattering angle
θ_B	Bragg angle
h	distance between two colloids
hkl	Miller indices
I	ionic strength
$I(\vec{q})$	scattered intensity
k	Boltzmann constant
κ^{-1}	Debye length
L	length of cylinder
L_g	gravitational length
λ	wavelength
m	deformation parameter
Δm	particle mass corrected for buoyancy
n_b	bulk number density
N_A	Avogdro's constant
$P(\vec{q})$	form factor
Π	osmotic pressure
$\vec{q}$	scattering vector
q	size ratio between depletant and superball
R	radius of cylinder
r	semiaxis of superball
r_1, r_2	semiaxes of superdisk
s	a parameter
$S(\vec{q})$	structure factor
T	temperature
V	volume
V_ov	overlap volume
ϕ	packing density
W_dep	depletion potential
x	height horizontal segment of cylinder
z	charge number